Abschlussbericht

Teilprojekt HZDR-IRE

„ GRUNDLEGENDE UNTERSUCHUNGEN ZUR IMMOBILISIERUNG LANGLEBIGER RADIONUKLIDE DURCH DIE WECHSELWIRKUNGEN MIT ENDLAGERRELEVANTEN SEKUNDÄRPHASEN“

Akronym: **ImmoRad**

Vorhabens-Nr.: **02NUK019D**

Teil I

Kurzbericht

Teil II

Eingehende Darstellung

Autoren: Dr. A. Scheinost

Dr. T. Dumas, Dr. R. Steudtner, Dr. S. Dulnee

Zuwendungsempfänger:

Helmholtz Zentrum Dresden Rossendorf e.V. (HZDR)

Institut für Ressourcenökologie (IRE)

Bautzner Landstrasse 400

01328 Dresden

Bundesministerium für Bildung und Forschung

Das diesem Bericht zugrundeliegende Vorhaben wurde mit Mitteln des Bundesministeriums für Bildung und Forschung unter dem Förderkennzeichen 02NUK019D gefördert.

Die Verantwortung für den Inhalt liegt bei den Autoren.

ABBILDUNGSVERZEICHNIS

1 Kurzbericht

1.1 Aufgabenstellung

Bei dem beantragten und durchgeführten Projekt mit dem Akronym ImmoRad *„GRUNDLEGENDE UNTERSUCHUNGEN ZUR **IMMO**BILISIERUNG LANGLEBIGER **RAD**IONUKLIDE DURCH DIE WECHSELWIRKUNGEN MIT ENDLAGERRELEVANTEN SEKUNDÄRPHASEN“* handelt es sich um ein Verbundprojekt mit sieben Partnern, namentlich dem Institut für Nukleare Entsorgung (KIT-INE), dem Institut für Mineralogie und Geochemie (KIT-IMG), dem Institut für Energie- und Klimaforschung (FZJ-IEK-6), dem Institut für Ressourcen Ökologie (HZDR-IRE), dem Institut für Geowissenschaften (GU-IFG), dem Labor für Endlagersicherheit, Schweiz (PSI-LES) und dem Departamento de Geología der Universität Oviedo, Spanien (UO-DG). ImmoRad wurde gefördert von dem Bundesministerium für Bildung und Forschung (BMBF).

Das Ziel des Vorhabens ist es einen Beitrag zur sicheren Endlagerung hochradioaktiven Abfalls zu leisten. In diesem Kontext soll ein auf atomarer Skala basierendes Prozessverständnis der Wechselwirkung von Actiniden und Spaltprodukten mit endlagerrelevanten Mineralen bzw. Mineraloberflächen erlangt werden, um so Retentionsmechanismen auf langen Zeitskalen zu verstehen.

Dazu sind die Forschungsaktivitäten und Expertisen der Partner im Rahmen des beantragten ImmoRad-Projektes gebündelt worden, um den Einfluss der Mischkristallbildung in wässriger Umgebung auf die Migration bzw. Rückhaltung von Radionukliden zu untersuchen.

Konkret sind die strukturellen, physikalischen und thermodynamischen Eigenschaften von endlagerrelevanten Verbindungen experimentell charakterisiert werden. Diese Arbeiten sind zwingend notwendig, um dann thermodynamische Modellrechnungen durchführen zu können, die wiederum die unverzichtbare Grundlage für eine Vorhersage des Langzeitretentionsverhaltens für Radionuklide bilden.

An drei relevanten Radionuklidgruppen:

1. **Dreiwertige Actinide Pu, Am, Cm (Einbau in und Wechselwirkung mit Phosphaten, Carbonaten, Eisen(hydr)oxiden, gelöste anorganische Spezies)**
2. **Vierwertige Actiniden Th, U, Np, Pu (Einbau in und Wechselwirkung mit Silicaten, Sulfaten, Carbonaten, Sulfiden, Eisen(hydr)oxiden, LDH-Phasen, Phosphaten)**

3. Radium und Spaltprodukte Se(IV), Se(VI), Tc (Einbau in und Wechselwirkung mit Sulfaten, Sulfiden, LDH Phasen, Carbonaten)

wurden die experimentellen Grundlagen zum Prozessverständnis der Bildung der Mischkristalle erarbeitet.

Die komplementären Expertisen der beteiligten Projektleiter, sowie die notwendige Infrastruktur für Arbeiten mit radioaktiven Materialien am KIT-INE, am HZDR-IRE, am PSI-LES und am FZJ-IEK6 bilden ideale Voraussetzungen, um diese Arbeitsziele zu erreichen. Die Partner, die über keine eigenen Kontrollbereiche verfügen, haben ihre experimentellen Arbeiten auf nicht radioaktive Isotope der Spaltprodukte konzentriert. Um eine flächendeckende Untersuchung aller Aspekte der drei erwähnten Radionuklidgruppen zu gewährleisten, lassen sich die Verbundpartner mit den entsprechenden Zielsetzungen wie folgt darstellen:

- **Karlsruher Institut für Technologie, Institut für Nukleare Entsorgung (KIT-INE)**

  Beitrag zur Radionuklidgruppe (1)

  Cm(III), Am(III) und Eu(III) dotierte Calcite werden synthetisiert und die Besetzung der unterschiedlichen „sites“ wird mit Hilfe der TRLFS quantifiziert. Aus diesen Daten werden Verteilungsgleichgewichte zwischen in die Kristallstruktur des Calcits eingebauten Ionen und sorbierten Spezies errechnet. Die maximale Beladung der Sekundärphase mit Actiniden wird aus diesen Daten extrapoliert werden.

  Mit dreiwertigen Actiniden und Lanthaniden dotierte Calcit Einkristalle werden nach ihrer Synthese an der Beamline in Argonne untersucht. Mit diesen Röntgen-Reflektometriemessungen wird die Struktur der Oberfläche der Calcitkristalle bestimmt. Darüber hinaus sollte es möglich sein, Strukturinformationen zu den in die ersten Lagen des Kristalls eingebauten Fremdionen zu erhalten.

  Die mit Radionukliden dotierten Carbonate werden hinsichtlich der Freisetzung der Fremdionen betrachtet. Dabei wird sowohl der Einfluss von Konkurrenz- Ionen auf das System als auch die Auswirkungen der physiko-chemischen Umgebung (pH Wert, Temperatur) untersucht.

  Beitrag zur Radionuklidgruppe (2)

  Th(IV) und Np(IV/V) dotierte Calcite werden im MFR (Mixed Flow Reactor) unter „steady state“ Bedingungen synthetisiert. Einbau sowie Freisetzung der Actiniden wird quantifiziert und modelliert. Der Einfluss von Fremd- Ionen auf die Bildung dieser An(IV): Calcit „solid solutions“ wird mit Hilfe von SEM und AFM untersucht. Durch die Anwendung spektroskopischer Methoden (XAS) werden die Strukturparameter der Einbauspezies bestimmt. Aus den erhaltenen Ergebnissen wird sich ein Prozessverständnis des Einbaus von vierwertigen Actiniden in Sekundärphasen auf molekularer Ebene ableiten lassen.

- **Karlsruher Institut für Technologie, Institut für Mineralogie und Geochemie (KIT-IMG)**

  Beitrag zur Radionuklidgruppe (3)

  Stabilität von Se-dotierten Fe-Sulfiden: Selen-dotierte Fe-Sulfide (Mackinawit, Pyrit) werden mit Hilfe unterschiedlicher Verfahren synthetisiert (Batch, Durchflussreaktor, Dampftransport). Die Konzentration und Speziation von Se in den Fe-Sulfiden wird mit Synchrotron- Methoden untersucht. In einer elektrochemischen Zelle werden die Se-dotierten Fe-Sulfide variablen Eh/pH-Bedingungen ausgesetzt, die ein realistisches Spektrum von natürlichen Systemen (anoxische Porenwässer des Opalinustons, oxische Grundwässer) widerspiegeln. Die Bestimmung der Selen- Speziationen und deren Konzentration im Mineral geben Aufschlüsse über die Stabilität von Se in Fe-Sulfiden unter schwankenden hydrochemischen Verhältnissen.

- **Forschungszentrum Jülich, Institut für Energie- und Klimaforschung, (FZJ-IEK6)**

  Beitrag zur Radionuklidgruppe (1)

  Die Möglichkeit, dass sowohl in Carbonat- als auch in Phosphatverbindungen zwei Ca^{2+}-Ionen durch Na^{+} und Eu^{3+} substituiert werden, soll mit Hilfe von quantenmechanischen Berechnungen abgeschätzt werden. Die Berechnungen basieren auf Bestimmungen der Überschussenergien von Superzellen der Typen Calcit/Aragonit und Apatit, in denen Paardefekte durch NaEu vorliegen. Aus den Überschussenergien der Defektstrukturen sollen thermodynamische Parameter zur Vorhersage der Eu(III)- Löslichkeit in Carbonaten und Phosphaten abgeleitet werden. Die durch Berechnung vorhergesagten Werte sollen durch spektroskopische Ergebnisse am KIT-INE verifiziert werden. Die quantenmechanischen Berechnungen werden am JuRoPa im FZJ in Kooperation mit dem UF-IFG durchgeführt.

  Beitrag zur Radionuklidgruppe (2)

  Mischkristallsysteme der vierwertigen Actiniden Th(IV), U)IV), Np(IV) und Pu(IV) als Phosphate werden mittels der Hydrothermalsynthese in Gegenwart von H_3PO_3 synthetisiert. Neben den Phosphaten sollen für das Actinidenpaar Th(IV) und U(IV) das Mischkristallsystem der Silikate ebenfalls synthetisch abgebildet werden. Das den tetravalenten Actiniden homologe Zr(IV) soll mittels der Methode der Co- Präzipitation in die LDH Schichtstruktur durch partielle Substitution von Mg(II) und Al(III) eingebracht werden. Zur Charakterisierung der strukturellen Nahordnung und zur Validierung der Valenzen der Actiniden sollten EXAFS/XANES und XPS Messungen durchgeführt werden. Hierzu können die Synchrotron Anlagen in Karlsruhe oder Grenoble genutzt werden. Das in Frankfurt befindliche Calvet-Type Kalorimeter bietet sich für detailliertere thermodynamische Untersuchung der Mischphasen an.

  Beitrag zur Radionuklidgruppe (3)

  Batchsorptionsversuche werden in der Nähe des thermodynamischen Gleichgewichts durchgeführt. Strontium- und Bariumsulfate mit unterschiedlichem Barium/Strontiumverhältnis (Synthese: Universität Oviedo) werden in Kontakt zu einer radiumhaltigen Lösung gebracht. Aufgrund der laut Literatur sehr unterschiedlichen Temperaturabhängigkeit der Löslichkeit der Endglieder ist auch eine Variation der Temperatur vorgesehen. Aus den Sorptionsdaten werden Verteilungsgleichgewichte für die jeweiligen Versuchsbedingungen ermittelt. Die erzeugten Mischphasen sollen dann in Bezug auf ihre Homogenität und Struktur mikroskopisch und/oder spektroskopisch untersucht werden (z.B. FIB = focused ion beam, REM, EXAFS).

  Parallel werden thermodynamische Berechnungen (ab-initio Modellrechnungen zur Wechselwirkung von Barium – Strontium –Radium im Sulfatsystem, ternäre „solid solution“ Berechnungen) genutzt, um die Versuchspunkte für die Experimente zu definieren und die Ergebnisse zu interpretieren. Die thermodynamischen Mischungseffekte im ternären (Ba, Sr, Ra)SO_4 System sollen mit der „Double Defect Methode“ untersucht werden. Die quantenmechanischen Berechnungen hierzu werden am Supercomputer JuRoPa im FZJ und an den Supercomputern „FUCHS“ und „LOEWE“ der Universität Frankfurt durchgeführt. Das durch Zusammenarbeit mit dem PSI und der Forschungsgruppe UNI-Oviedo abgeleitete thermodynamische Model soll dann in das geochemische Modell GEMS (PSI) implementiert werden. Die Kombination von theoretischen Berechnungen und experimentellen Ergebnissen soll letztlich ermöglichen, den Einfluss von Barium und Strontiumsulfat auf die Rückhaltung von Radium quantitativ zu beschreiben und, soweit möglich, das System auf einer thermodynamischen Grundlage zu definieren.

- **Helmholtz-Zentrum Dresden-Rossendorf, Institut für Ressourcen Ökologie (HZDR-IRE)**

  Beitrag zur Radionuklidgruppe (1)

  Das IRE wird die mögliche Inkorporation von Pu(III) in Magnetit und ein Fe-Carbonat (Siderit oder Chukanovit) untersuchen, basierend auf der langfristigen Equilibrierung (2 Jahre) von Pu(III) und Pu(V) mit diesen Mineralen, im Vergleich zu frisch gefällten Pu(III)/Fe(II)/Fe(III)/Carbonat Kopräzipitaten. Die Struktur und Oxidationsstufe der mit der Festphase assoziierten Pu-Spezies wird spektroskopisch (XAFS) untersucht, und die Lösungsbedingungen (Eh, pH, gelöste Ionen) werden sorgfältig erfasst, um Stabilitätskonstanten der Pu(III)-Sorptionskomplexe und Festphasen zu bestimmen. Da zwei entsprechende Proben seit Anfang 2010 equilibriert werden, können innerhalb der Projektdauer auch Zeitskalen jenseits von 2 Jahren untersucht werden.

  Beitrag zur Radionuklidgruppe (2)

  Das IRE wird die reduktive Reaktion von Np(V) mit Mackinawite (FeS) und Magnetit systematisch untersuchen. Die Reaktionsprodukte werden mit Np(IV)/Fe(II)/S(-II) und Np(IV)/Fe(II)/Fe(III)/O(-II) Kopräzipitaten verglichen. Durch die Reaktion mit Mackinawit kann auch die bisher vorwiegend bei tieferen Redoxstufen beobachtete Sulfid-koordination von Np(IV) verifiziert werden. Außerdem wird das IRE die mögliche Inkorporation von Np(IV) durch die Fe(II)-Carbonate Siderit oder Chukanovit untersuchen, sowohl im Langzeit-Sorptionsexperiment (2 Jahre) als auch an Actinid/Fe(II)/Karbonat Kopräzipitaten. Wie oben werden die Struktur und Oxidationsstufe der mit der Festphase assoziierten Np-Spezies spektroskopisch (XAFS, eventuell auch XPS) untersucht, und die Lösungsbedingungen (Eh, pH, gelöste Ionen) werden sorgfältig erfasst, um Stabilitätskonstanten der Sorptionskomplexe und Festphasen zu bestimmen.

  Beitrag zur Radionuklidgruppe (3)

  Das IRE wird die von PSI-LES hergestellten „solid solutions“ zwischen Se(IV/VI) und LDH und Tc(VII) und LDH, sowie die von KIT-IMG hergestellten „solid solutions“ zwischen Se und Eisensulfiden mittels der eigenen XAFS-Beamline ROBL auf Oxidationsstufen und Nahordnung untersuchen.

- **Universität Frankfurt, Institut für Geowissenschaften (UF-IFG)**

  Beitrag zur Radionuklidgruppe (1)

  Cm-haltige Verbindungen sind in der Vergangenheit von uns mit DFT-Rechnungen untersucht worden. Diese Rechnungen sollen nun auf Verbindungen, die hier relevant sind, ausgedehnt werden. Darauf aufbauend sollen thermodynamische Modelle erstellt werden.

  Beitrag zur Radionuklidgruppe (2)

  Vierwertige U-haltige Phasen sollen in Frankfurt kalorimetrisch und schwingungsspektroskopisch charakterisiert werden.

  Beitrag zur Radionuklidgruppe (3)

  Unsere DFT-basierten Modellrechnungen an Se-haltige Phasen sollen fortgesetzt und ausgedehnt werden. Proben aus anderen Gruppen sollen mit Mikrokalorimetrie und Raman-Spektroskopie charakterisiert werden.

- **Paul Scherrer Institut, Labor für Endlagersicherheit, Schweiz (PSI-LES)**

  Beitrag zur Radionuklidgruppe (3)

  Das PSI-LES wird „screening“ Sorptionsversuche an verschiedenen LDH Phasen durchführen und die relevanten Se(IV) – LDH und Tc(VII) – LDH Mischkristalle herstellen und mittels nasschemischer Methoden, XRD und XAFS Spektroskopie charakterisieren. Zudem wird die thermodynamische Mo-

dellierung der oben erwähnten festen Lösungen mittels „forward and inverse modelling“ der experimentellen Daten und unter Verwendung des PSI GEM-Selektor-3 Code durchgeführt. Mittels nasschemischer und spektroskopischer Untersuchungen wird der Einfluss von reduzierenden Bedingungen auf die Stabilität der “solid solutions“ und den Redoxzustand der in den „solid solutions“ eingebauten Anionen bestimmt. Die XAFS Untersuchungen werden in Zusammenarbeit mit HZDR-IRE durchgeführt.

Dr. Curti und Dr. Kulik werden zu der Modellierung der nasschemischen Daten beitragen. Dieses Ziel soll hauptsächlich mit Hilfe des PSI GEM-Selektor-3 Codes erreicht werden.

Übergreifend:

Nasschemische und spektroskopische Daten sollen durch eine konsistente thermodynamische Modellierung zusammengeführt und quantitativ beschrieben werden. Um solche Daten in geochemische Modelle zu implementieren sind spezielle Programme notwendig wie z.B. der am PSI-LES entwickelte GEM-Selektor-3 Code. Es ist vorgesehen, einen „Short Course“ für alle Teil-nehmer des Verbundprojekts am PSI (Leitung: Dr. Kulik) zu organisieren mit dem Schwerpunkt auf einer effizienten Verwendung des GEM-Selektor-3 Programms in Hinblick auf die Modellierung projektrelevanter Systeme, insbesondere von „multi-site“ festen Lösungen wie z.B. LDH Phasen. Ein anderer Schwerpunkt werden die Arbeiten zur Bestimmung thermodynamischer Parameter aus atomistischer Simulationen sein (zusammen mit Dr. Vinograd).

- **Universidad de Oviedo, Departamento de Geología, Spanien (UO-DG)**

  Beitrag zur Radionuklidgruppe (3)

  Reaktive Sulfat Diffusion durch gel-gefüllte Säulen mit definiertem Sr/Ba Verhältnis in der Porenlösung:

  Agar-Agar oder Silica- Hydrogel kommt in den Säulen zum Einsatz. Das Sr/Ba Verhältnis wird im Vorhinein festgelegt, um Kristalle einer definierten Zusammensetzung zu erzeugen. Die Übersättigung im System wird so eingestellt, dass die Entwicklung von Konzentrationsgrenzschichten Minimal gehalten werden kann.

  Präzipitations-Alterungs-Experimente bei epithermalen Bedingungen:

  Durch schnelle Präzipitation bei Umgebungsbedingungen können homogene Mischkristalle erzeugt werden. Allerdings sind die Präzipitate oft flockig und mikrokristallin. Um dieses Problem zu vermeiden, kommen Batch- und Durchflussreaktoren bei 100° - 140°C zum Einsatz. Das Ziel ist die Qualität und Größe der gebildeten Kristalle zu verbessern und den Einfluss der Temperatur auf die Homogenität der Kristalle zu untersuchen.

  Einbau von SeO_4^{2-} als Substituent für SO_4^{2-} in (Ba,Sr)SO_4 Mischkristallen:

  Die Löslichkeit von (Ba,Sr)SO_4 Mischkristallen nimmt mit dem Sr-Gehalt zu. Ziel der Untersuchung ist das Sr/Ba Verhältnis zu finden bei dem der Se(VI) Einbau in (Ba,Sr)(SO_4,SeO_4) maximal ist. Das experimentelle Protokoll sieht Präzipitationsversuche in einem Lösungskalorimeter und Kristallwachstumsexperimente durch Gegendiffusion der Reaktanden in einer Gel-Säule vor. Die Präzipitationsexperimente dienen der Quantifizierung der thermodynamischen Mischungsparameter: Mischungsenthalpie und Excess- Mischungsvolumen. Die Ergebnisse werden mit Daten aus molekularen Simulationen verglichen. Durch die Kristallwachstumsexperimente wird das effektive Kristallisationsverhalten untersucht und es werden Kristalle mit Durchmessern im Millimeterbereich erzeugt, die für die strukturelle Charakterisierung herangezogen werden können.

Einbau von Se(VI) in Zementphasen:

Das Mineral Ettringit, $Ca_6Al_2O_6(SO_4)_3 \cdot 26H_2O$, ist eine Phase, die während der frühen Hydratation von Portland Zementen gebildet wird. Die Kristallstruktur dieses Minerals toleriert den Einbau verschiedener Oxyanionen, z.B. $HAsO_4^{2-}$ und SeO_4^{2-}. Es konnte gezeigt werden, dass SeO_4^{2-} in der Ettringitstruktur Sulfat ersetzt. In welchem Ausmaß dieser Austausch stattfinden und was die thermodynamischen Eigenschaften von $Ca_6Al_2O_6(SeO_4,SO_4)_3 \cdot 26H_2O$ sind ist jedoch kaum bekannt. Die Mischbarkeit der Endglieder dieser Mischkristallreihe wird durch Kristallisationsexperimente quantifiziert. Die Experimente werden in einer Stickstoff Handschuhbox durchgeführt, um Kontaminationen mit CO_2 zu vermeiden. Die resultierenden Festphasen werden in verschiedenen Stadien des Alterungsprozesses auf ihre Zusammensetzung und Struktur hin untersucht. Besondere Aufmerksamkeit gilt dabei der Bestimmung einer möglichen Mischungslücke. Die Bestimmung der Grenzen der Mischbarkeit erlaubt es die thermodynamischen Mischungsparameter durch ein sub-reguläres Solid-Solution Modell zu beschreiben.

Kopräzipitation von Se(VI) mit $CaCO_3$:

Die Kopräzipitation tetraedrischer Oxyanionen mit $CaCO_3$ erfolgt durch Anionensubstitution in der Kristallstruktur. Dieser Effekt wurde kürzlich für SO_4^{2-} Ionen beschrieben. Der Einbau von Sulfat in $CaCO_3$ fördert die metastabile Bildung von Vaterit anstelle von Calcit. Während des Alterungsprozesses löst sich Vaterit auf und Calcit bildet sich. Bei hohen Sulfatbeladungen, wird der sulfathaltige Vaterit jedoch stabilisiert und vollzieht keine sekundäre Umwandlung. Die Anfangshypothese dieses Teilprojektes ist, das Selenat bei der Kopräzipitation mit $CaCO_3$ eine ähnliche Rolle spielen kann wie Sulfat. Das experimentelle Protokoll wird dabei wieder eine Kombination aus Präzipitations- und Gegendiffusionsexperimenten umfassen. Das Ziel ist es die Mischbarkeit von Se(VI) mit Calcit und Vaterit und die Stabilität des Se(VI)-haltigen Vaterits zu bestimmen.

1.2 Voraussetzungen, unter denen das Vorhaben durchgeführt wurde

Das Projekt hatte eine reguläre Laufzeit von drei Jahren (01.02.2012 – 31.01.2015) und wurde dann kostenneutral verlängert bis zum 30.09.2015. Der Gesamtumfang der beantragten Finanzierung des **(HZDR-IRE)** lag bei **362.626,63 Euro.** Davon entfielen

221.890,91 € auf Personalkosten

2.866,39 € auf Materialkosten

29.721,53 € auf Reisemittel

Mit Datum vom 11.01.2012 wurde mittels Zuwendungsbescheid das Institut für Ressourcenökologie (HZDR-IRE) über den Antrag vom 06.12.2011 und über die Höhe der Zuwendung aus dem Bundeshaushalt und am 28.11.2013 mittels Änderungsbescheid über die neue kassenmäßige Mittelabführung informiert. Die Höhe der Zuwendung lag bei **400.943,00 Euro** und das Förderkennzeichen lautet: **02NUK019D**, (Kassenzeichen: 810302576437).

Das Projekt konnte unter sehr guten Voraussetzungen gestartet werden und die Ziele des Forschungsvorhabens konnten größtenteils erreicht werden.

1.3 Planung und Ablauf

Mit Datum vom 11.01.2012 wurde das Institut für Ressourcenökologie, über die Zuwendung aus dem Bundeshaushalt informiert. Die Projektlaufzeit (Bewilligungszeitraum) von drei Jahren wurde im Zuwendungsbescheid fixiert: 01.02.2012-31.01.2015. Dann erfolgte eine kostenneutrale Verlängerung bis zum 30.09.2015.

Der Beginn der geplanten Arbeiten verzögerte sich durch Schwierigkeiten geeignetes Personal für die Bearbeitung der Forschungsaufgaben zu finden, um einen Monat. Die Ziele des Forschungsvorhabens wurden innerhalb der kostenneutralen Verlängerung erreicht.

1.4 Wissenschaftlich-technischer Stand, an dem angeknüpft wurde

The disposal of nuclear waste in deep geological formations behind multiple barriers is a concept favored by many nuclear power producing countries to ensure a lasting protection of people and the environment. The multiple barrier system consists of three principal parts, an engineered barrier (copper or stainless steel containers), a geo-engineered barrier (cement or clay-based backfill-material, e.g. bentonite) and the geological barrier (argillaceous, granitic or salt host rock).[1] Many of these components contain or form Fe^{II}-bearing minerals, which may act as scavenger for potentially released radionuclides by their reducing power and sorption capacity. Steel containers are likely to corrode under near-field conditions, forming for instance magnetite, siderite, chukanovite and Fe-phyllosilicates in contact with clay backfill, [2, 3] magnetite and hydrous Fe^{II} oxides in contact with brine, [4] and Fe^{II} sulfides in the presence of sulfate reducing bacteria (Figure 1). [5] Such Fe^{II}-bearing minerals also occur naturally in clay rocks; e.g. MX80 bentonite considered as backfill material contains 0.7 % siderite and 0.3% pyrite, and Opalinus clay considered as host rock in Switzerland contains 6% siderite and 0.9% pyrite. [6, 7]

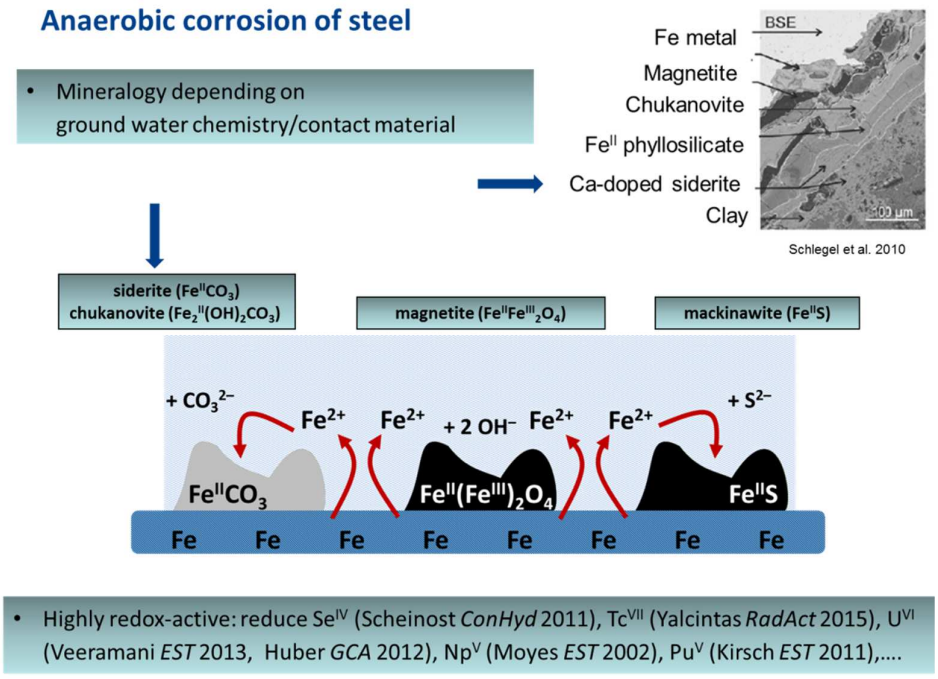

Figure 1: Anoxic steel corrosion processes.

Spent nuclear fuel consists mainly of the original uranium dioxide (~95%) and its fission products (lanthanides, technetium, selenium, noble gases and cesium, ~4%). Neutron absorption and decay reactions lead to the formation of plutonium isotopes (~1%) and the minor actinides neptunium, americium and curium (<0.1% of typical burnt fuel). The redox-sensitive elements uranium, plutonium, technetium, selenium have been shown to be efficiently immobilized by sorption and redox reactions on Fe^{II}-bearing minerals [4, 8-14]

Plutonium is the major transuranium actinide in civil and military nuclear waste. It is of environmental concern because of its high radiotoxicity and the long half-life of relevant nuclides (^{239}Pu: 24 100 a, ^{242}Pu: 375 000 a, ^{244}Pu: $8.0 \cdot 10^7$ a).[15] The solubility and complexation behavior of plutonium in aqueous systems and therefore its environmental fate are highly oxidation state dependent.[16] Due to its predominance over a wide pe/pH range and the possibility of colloid formation,[17, 18] PuO_2 is considered one of the most important solids for Pu risk assessment. Under reducing conditions in the acidic to neutral pH range and particularly in presence of dissolved Fe(II) or Fe(II)-bearing minerals Pu(III) is, however, relevant and compared to Pu(IV) often forms much more soluble species (Figure 2).[19, 20]

Sorption of Pu(V) to hematite, goethite and magnetite was found to be accompanied by surface mediated reduction to Pu(IV).[21-25] While the reductive capacity of the Fe(II)-Fe(III) mixed valence spinel magnetite is well known,[26, 27] the reduction of Pu(V) with iron(III) minerals hematite and goethite was attributed to the presence of traces of Fe(II) or to a stabilization of solid-state Pu(IV).[21] Recently, we investigated the sorption of Pu(V) to magnetite, chucanovite and mackinawite under strictly anoxic conditions. [11] Pu(V) was reduced in presence of all three minerals. A newly identified, highly specific Pu(III)-sorption complex was formed with magnetite. Solid PuO_2 phases were formed in the presence of mackinawite and chukanovite; in the case of chukanovite, up to one third of plutonium was present as Pu(III). This highlights the necessity to consider under reducing anoxic conditions Pu(III) species in addition to tetravalent PuO_2 for risk assessment.

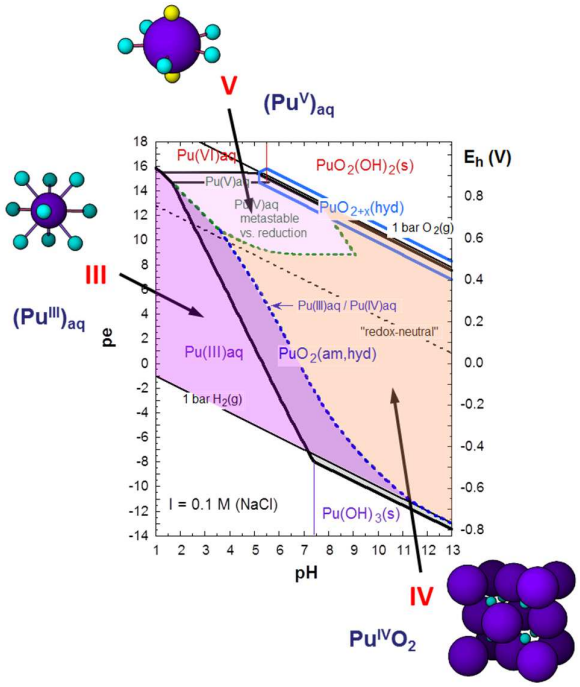

Figure 2. Pourbaix diagram for [Pu] = 10^{-5} M in 0.1 M NaCl. Note that the redox cascade produces first soluble species (oxidation states V and VI), then an insoluble species (oxidation state IV), and then again a soluble species (oxidation state III). For construction of the full black lines, PuO_2(am,hyd) is the considered Pu^{IV} equilibrium species. Dashed lines result from use of Pu^{IV}aq instead of PuO_2(am,hyd) as redox partner for Pu^{III}aq (purple) or Pu^{V}aq (pink). The dark purple shaded area highlights the increase of the Pu^{III}aq predominance field when Pu^{IV}aq instead of solid PuO_2(am,hyd) is the redox partner for Pu^{III}aq.

However, sorption and precipitation of PuO_2-like phases may not be the only relevant retention process for Pu in presence of Fe(II)-bearing minerals; structural incorporation may be an additional pathway, which may lead to a higher recalcitrance against especially oxidative dissolution. While up to now this has not been investigated for Pu, several lines of evidence exist based on lanthanides. Up to 2 % of Ln^{III} were incorporated during microbial magnetite formation. [28] Furthermore, Sm, Eu, and Gd-doped magnetite nanoparticles have been synthesized. [29] Both works demonstrate that magnetite was the only solid phase present, but they do not give direct evidence that and how the lanthanoides are incorporated by magnetite. Since the ionic radius of Pu^{III} in octahedral coordination (1.14 Å) is very similar to that of Ln^{III} (1.17 Å), Sm^{III} (1.10 Å), Eu^{III} (1.09 Å), Gd^{III} (1.08 Å), one would expect a similar incorporation mechanism for Pu(III). In contrast, Ce^{III} (1.15 Å) was not incorporated by green rust/magnetite. [30]

Furthermore, penta- and hexavalent actinoides seem to be compatible with Fe oxide phases. For instance, up to 4 atom-% of U^{VI} were incorporated by hematite; there was no evidence for the uranyl-unit by IR, XANES-line shape and EXAFS distances in line with an uranate-like local coordination. [31, 32] Goethite and magnetite incorporated U^{V} as uranate (0.90 Å).[33-35] In contrast to trivalent Pu, however, the ionic radius of uranate is smaller (0.90 Å), hence more likely to fit.

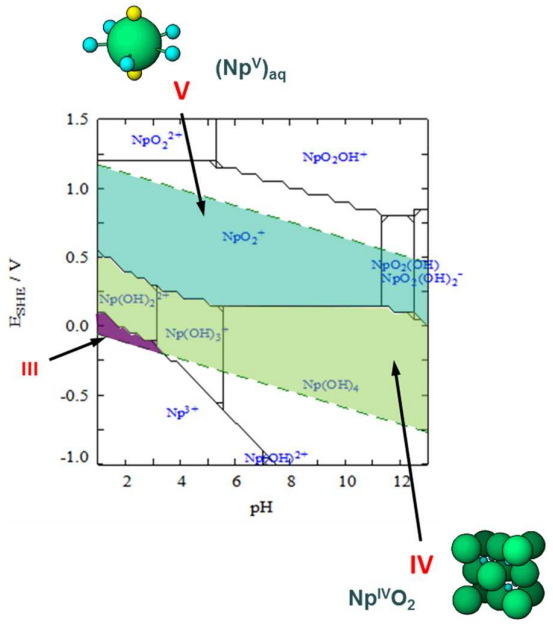

Figure 3. Pourbaix diagram for [Np] = 10^{-5} M in 0.1 M NaCl.

In contrast to Pu, the stability field of Np is dominated by the pentavalent and tetravalent oxidation states, while the trivalent oxidation state plays a much lesser role (Figure 3). Much less work has been conducted on the redox-driven (anoxic) immobilization of Np, although its major radionuclide ^{237}Np has a very long half life (2.14 Mio years) and contributes significantly to the long-term radiotoxicity of spent fuel. Work attempting to elucidate the mechanisms of Np reduction by mineral surfaces is even more scarce. Np^{V} was found to be much more strongly retained by magnetite under anoxic conditions than under atmospheric conditions; using a liquid extraction technique, Np associated with the solid phase was determined to be tetravalent. [36] In comparison to reduction by aqueous Fe^{II}, reduction by magnetite was 3 orders of magnitude faster. [37] A pioneering study employing EXAFS spectroscopy showed that Np^{V} was only weakly taken up by mackinawite, forming rather surprisingly a mononuclear Np^{IV} sorption complex coordinated to both O and S. [38] In the presence of green rust, Np^{V} was rapidly

sorbed and reduced to Np^{IV} at the edges of the hexagonal platelets; the authors suggest formation of Np^{IV} particles, but their identification by TEM remained elusive. [39] Np^{V} reacted with Opalinus clay was reduced to Np^{IV} and showed a strong association with pyrite particles embedded in the clay matrix; the exact nature of the reduced Np^{IV} could not be identified, but the authors excluded formation of NpO_2 due to the absence of Np-Np backscattering contributions in Np L_3-edge EXAFS spectra. [40] Biotite and chlorite with structural Fe^{II} fully reduced Np^{V} to Np^{IV}, and nanoparticulate NpO_2 formed as identified by EXAFS. [41] In the presence of Ti-doped magnetite, sorption of Np was high at pH values 5 and 7, while the sorption at pH 3 was low, but increased with Ti-doping most likely because of the increasing Fe^{II} fraction to counterbalance the charge of structural Ti^{IV}. Using Np L_3-edge XANES and EXAFS, the reaction product could be identified as a Np^{IV} species, while the absence of Np-Np backscattering contradicted formation of NpO_2. [42] The authors claim formation of an inner-sphere sorption complex, but fitted Np-Fe and Np-Ti coordination numbers between 5 and 7 would rather suggest structural incorporation by magnetite or a secondary Fe phase. In conclusion, the few studies on Np uptake by Fe^{II}-bearing minerals under anoxic conditions show sorption and reduction to Np^{IV}, but the reaction mechanism and the end product, *i.e.* sorption complexation vs. structural incorporation vs. NpO_2 precipitation, often remain elusive.

1.5 Zusammenarbeit

HZDR-IRE hat im Verbundprojekt „Immobilisierung langlebiger Radionuklide durch die Wechselwirkungen mit endlagerrelevanten Sekundärphasen (Akronym: ImmoRad) mit den Verbundpartnern KIT-INE, KIT-IMG und PSI-LES zusammengearbeitet. Die Arbeiten von Dr. Thomas Dumas, Dr. Robin Steudtner und Dr. Siriwan Dulnee wurden hauptsächlich am HZDR und an der HZDR-eigenen Rossendorf Beamline an der ESRF in Grenoble durchgeführt. Allerdings war Dr. Dumas vom 1. bis 10.05.2012, vom 23. bis 27.04.2012 und vom 18. bis 23.11.2012 am INE in Karlsruhe, wo er gemeinsam mit David Fellhauer Arbeiten zum Einschluss von Pu in Magnetit durchführte. Dr. Henar Rojo-Sanchez (PSI-LES) war mehrmals an der HZDR-eigenen Rossendorf Beamline an der ESRF in Grenoble, um Messkampagnen durchzuführen. Ebenso haben Nicolas Boersig und Sebastian Potsch (KIT-IMG) einen einmonatigen Mess- und Auswerteaufenthalt an der Rossendorf Beamline verbracht.

Die wissenschaftlichen Ergebnisse wurden auf Statusseminaren/Workshops diskutiert (Tabelle 1).

Tabelle 1: Zusammenstellung der wichtigsten wissenschaftlichen Ereignisse innerhalb der Projektlaufzeit.

Datum	Ort	Anlass	Teilnehmer
02.04.12-03.04.12	Bad Herrenalb	Kick-off Meeting	A. Scheinost T. Dumas
18.02.13-19.02.13	Frankfurt	1. Statusseminar	A. Scheinost R. Steudtner
19.02.13-22.02.13	Frankfurt	Solid-Solution Workshop	R. Steudtner
13.05.14-16.05.14	Oviedo (Spanien)	2. Statusseminar	R. Steudtner
23.04.15-24.04.15	Villingen (Schweiz)	Abschluss-Seminar	A. Scheinost

2. Eingehende Darstellung

2.1 Verwendung der Zuwendung, erzielte Ergebnisse, Gegenüberstellung mit vorgegebenen Zielen

2.1.1 Verwendung der Zuwendung

Unter der Projektleitung von Herrn Dr. habil. Andreas Scheinost, Helmholtz-Zentrum Dresden-Rossendorf, Institut für Ressourcen Ökologie (HZDR-IRE), wurden die Arbeiten für das Verbundprojekt Immo-Rad durchgeführt.

Hier standen Personal-, Reise- und Sachmittel zur Verfügung, die wie folgt verwendet wurden.

2.1.1.1 Personalmittel

Die Personalmittel wurden für eine Postdoktoranden- Stelle verwendet, die bis 31.12.2012 von Dr. Thomas Dumas besetzt wurde. Da Herr Dumas ab 1.1.2013 auf eine feste Anstellung beim CEA wechseln konnte, wurde die Stelle mit Dr. Robin Steudtner bis zum Projektende besetzt. Außerdem wurden zwei Doktorierende beschäftigt, um die aufwändigen Laborarbeiten zu unterstützen und PHREEQCE-Modellierungen durchzuführen (Frau Annika Maffert von Oktober bis einschließlich Dezember 2013, Frau Siriwan Dulnee von April bis einschließlich Oktober 2014).

2.1.1.2 Reisemittel

Reisemittel wurden dazu verwendet, um zu den regelmäßig stattfindenden Arbeitstreffen des Verbundprojektes zu gelangen; außerdem für die Messaufenthalte von Herrn Dumas am HZDR und KIT, für die Messaufenthalte von Herrn Steudtner an der HZDR-eigenen Rossendorf Beamline in Grenoble (Frankreich), und schließlich für einen PHREEEQCE-Kurs von Frau Dulnee in Amsterdam. Außerdem wurden Reisen auf internationale und nationale Konferenzen unternommen, um die Ergebnisse einem breiteren Publikum vorzustellen und im internationalen Kontext zu diskutieren.

Eine exakte Auflistung der Dienstreisen befindet sich Tabelle 2.

Tabelle 2: Auflistung der Dienstreisen.

Reiseziel	Zeitraum	Reisende
Treffen: ImmoRad-Verbundprojekt		
Kick-off Meeting, Bad Herrenalb	02.04.12-03.04.12	A. Scheinost T. Dumas
Projektkoordinierung PSI-HZDR	25.04.-27.04.2012	A. Scheinost
1. Statusseminar und Solid-Solution Workshop, Frankfurt	17.02.13-22.02.13	A. Scheinost R. Steudtner
2. Statusseminar, Oviedo	13.05.14-16.05.14	R. Steudtner
Abschluss- Seminar, Villingen	23.04.15-24.04.15	A. Scheinost
Konferenzen		
Goldschmidt Conference 2012, Montreal	23.06.12– 30.06.12	A. Scheinost
Advanced Techniques in Actinide Spectroscopy (ATAS), Dresden	04.11.12– 11.11.12	T. Dumas
10. Projektstatusgespräch beim Projektträger Karlsruhe	09.11.12 – 14.11.12	A. Scheinost
ANAKON 2013, Essen	04.03.13– 07.03.13	R. Steudtner
Goldschmidt Conference 2013, Florence	25.08.13– 30.08.13	A. Scheinost R. Steudtner
GdCh Tagung, Darmstadt	01.09.13– 04.09.13	R. Steudtner
International Conference on the Chemistry and Physics of the Actinide Elements, Karlsruhe	21.07.13– 26.07.13	A. Scheinost
American Chemical Society, Fall Meeting 2014, San Francisco, USA	08.08.14– 23.08.14	A. Scheinost
Actinide-XAS, Villigen, Switzerland	22.04.14– 24.04.14	A. Scheinost
Goldschmidt Conference 2015, Prague, CZ	15.08.15 -22.08.15	R. Steudtner A. Scheinost
GdCh Wissenschaftsforum, Dresden	31.08.15 – 02.09.15	R. Steudtner
Kurse		
PHREEQC Course, Amsterdam	01.04.12 – 07.04.12	S. Dulnee
Externe Messkampagnen		
Kopräzipitationsexperimente am HZDR-IRE	19.03.12 – 30.03.12	T. Dumas
Kopräzipitationsexperimente am KIT-INE	01.05.12 – 10.05.12	T. Dumas
Kopräzipitationsexperimente am KIT-INE	18.11.12 – 23.11.12	T. Dumas
EXAFS-Messungen an ROBL (ESRF, Grenoble)	05.06.13 – 11.06.13	R. Steudtner
EXAFS-Messungen an ROBL (ESRF, Grenoble)	08.12.13 – 11.12.13	R. Steudtner
EXAFS-Messungen an ROBL (ESRF, Grenoble)	29.04.14 – 06.05.14	R. Steudtner
EXAFS-Messungen an ROBL (ESRF, Grenoble)	29.01.15 – 01.02.15	R. Steudtner S. Lehmann

2.1.1.3 Sachmittel

Die zur Verfügung stehenden Sachmittel wurden für den Kauf von Verbrauchsmaterialien und Chemikalien verwendet.

2.1.2 Erzielte Ergebnisse

2.1.2.1 Molecular mechanisms of Pu reductive sorption and precipitation with magnetite

We prepared two Pu-doped samples containing 1000 and 3600 mg/kg Pu under anoxic conditions in an Ar-atmosphere glovebox by coprecipitation. For this, the appropriate amount of ^{242}Pu(V) was added to a 1.2 M Fe chloride solution with an Fe(II)/(III) ratio of 0.5. Uv-vis spectroscopy showed an immediate reduction of Pu(V) to Pu(III), hence we had to abandon our original plan to produce both Pu(V) and Pu(III)-doped magnetites, but could only proceed with Pu(III)-doped magnetite. Magnetite precipitation was then induced by pouring this mixed Pu/Fe solutions rapidly into caustic. The resulting black suspension was split in two parts. The first part was centrifuged and washed two times to obtain the solid for XRD, TEM and XAFS analysis ("fresh samples"). The other half of the suspensions was used for an Fe(II)-induced aging procedure by adding 0.45 M $FeCl_2$ and stirring the suspensions for one week under anoxic conditions. [33] The suspensions were then centrifuged and washed two times to obtain the solid for XRD, TEM and XAFS analysis ("aged samples").

XRD analysis of the resulting four samples (fresh and aged for both 1000 and 3600 mg/kg Pu loading) showed the presence of magnetite only, with the cubic space group Fd3m and a c=8.397Å. The broad lines indicate monocrystalline material, in line with the HR-TEM images showing domain sizes of about 5 nm (Figure 4). Furthermore, the XRD line widths are independent of Pu loading and aging. The Fe(II) fraction in relation to Fe_{total}, which would be ideally 33 % for stoichiometric magnetite (Fe_2O_3), was 32.4 % for the 1000 mg/kg sample, and 30.4 % for the 3600 mg/kg sample. Nominally, one would expect 32.8 % and 32.3 %, respectively, when taking into account the two electron reduction step from Pu(V) to Pu(III). Therefore, the magnetite Fe(II)/Fe(III) ratios is understoichiometric as expected from the Pu reduction (1000 ppm sample) or slightly more understoichiometric for the 3600 ppm sample.

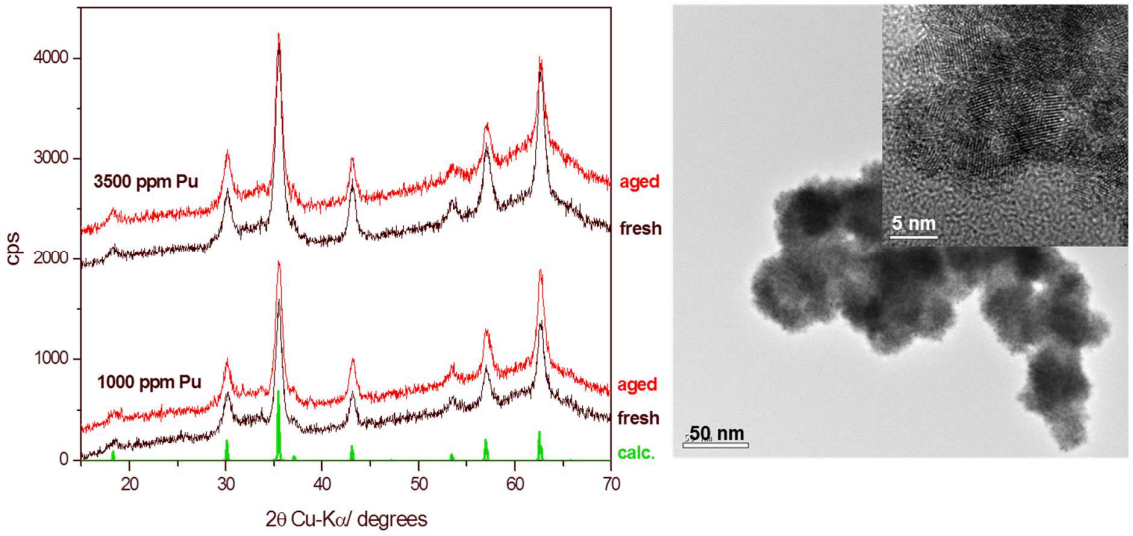

Figure 4: XRD patterns of magnetite with two different Pu doping levels after precipitation ("fresh"), after Fe(II)-induced aging ("aged"), and after calcination ("calc."). The right side shows TEM micrographs of the aged 3500 ppm Pu sample.

To investigate the oxidation state and local structure of Pu in magnetite, we employed Pu L_{III}-edge XAFS spectroscopy. The XANES part confirmed that Pu associated with the solid phase was trivalent, as expected from the presence of Pu(III) already in the initial Fe(II)/Fe(III) solution (Figure 5). In contrast to the long-range structure probed by XRD, the EXAFS part (**Figure 6**) showed a clear aging effect of the local structure around Pu. Iterative Transformation Factor Analysis (ITFA) [43] suggested two spectral components, i.e. two structurally different chemical species.

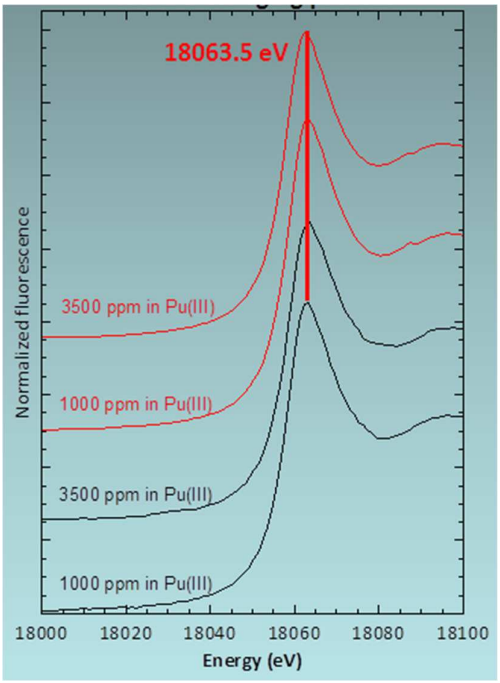

Figure 5: Pu L_{III} XANES spectra of magnetite with two different Pu doping levels. Black traces are of fresh precipitates, red traces are of Fe(II)-induced mineral aging.

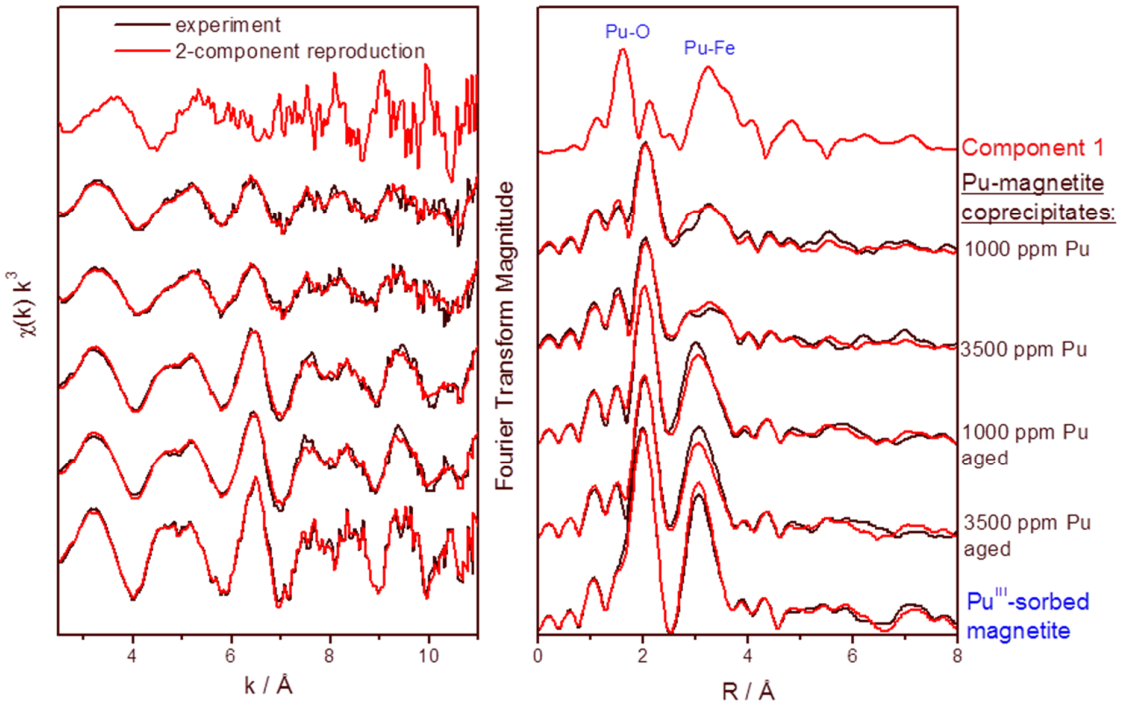

Figure 6: Pu L_{III} EXAFS spectra of the four different Pu-doped magnetite samples and of a Pu(III) magnetite sorption sample. Black traces are experimental data, red traces are their reconstruction by two principal components.

We then added the spectrum of a sorption sample aged for 2 years (labelled "Pu sorbed magnetite" in **Figure 6**). The spectrum of this sample was identical to the previously published sorption complex, a tridentate Pu(III) inner-sphere sorption complex on the magnetite {111} faces, demonstrating that long-term sorption did not alter the sorption complex, nor did it led to a structural incorporation. [11]

The ITFA-derived number of components remained still two, indicating that this sorption complex is present in the coprecipitation samples.

Using the iterative target test module of ITFA, we could then extract the spectrum of the second species (labeled “component 1” in **Figure 6**). This extracted spectrum could be fitted with two Pu-O shells of about 6 oxygen atoms, and two Pu-Fe shells at 3.61 and 3.97 Å (**Figure 7**). As the comparison with the magnetite Oh site shows, are all distances around Pu expanded. The coordination numbers of the two Pu-Fe shells are about 3, hence only half of those of the Oh site, similar to the tridentate sorption complex shown below. In contrast to the 9-fold oxygen coordination of the sorption complex, however, the oxygen coordination is only 6-fold and split into two distances of 2.23 and 2.6 Å. This strongly suggests incorporation of Pu(III) into the magnetite structure, causing a strong distortion of the Oh site because of the much larger diameter of Pu(III) (1.15 Å) in comparison to the diameter of Fe(III) (0.79 Å).

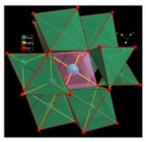

Pu^{III} incorporated

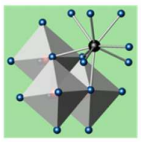

Pu^{III} sorbed

	EXAFS				Magnetite Oh site		
	path	CN	R / Å	σ^2 / Å^2	Path	CN	R / Å
Comp. 1	Pu-O	2.5	2.23	0.005	Fe-O	6	2.06
	Pu-O	3.9	2.46	0.005			
	Pu-Fe	2.6	3.61	0.010	Fe-Fe	6	2.97
	Pu-Fe	3.2	3.97	0.010	Fe-Fe	6	3.48
Comp. 2	Pu-O	9	2.45				
	Pu-Fe	3	3.54				
	Pu-Fe	3	4.20				

Figure 7: Pu L_{III} EXAFS shell fit data of the two principal components shown in **Figure 6**.

We subsequently determined the fractions of the two Pu species in the four Pu-magnetite coprecipitation samples using ITFA (**Figure 8**). While before the aging, about 2/3 of Pu is hosted by the heavily distorted Oh site of magnetite independent of Pu-loading, this goes down to about 1/3 after aging. Therefore, the fraction of the sorption complex increases with aging, suggesting that the sorption complex is the thermodynamically stable species and not the incorporated species. The total process can hence be described as kinetic entrapment of the structurally incompatible Pu(III) cation during the rapid precipitation of the magnetite phase, which is expelled from the structure with time. Therefore, for the longterm modelling for the safety case, the sorption species is more relevant, while structural incorporation may play a role only during the active corrosion process. We also determined the Pu concentration by liquid scintillation counting (LSC). In all cases (2-year sorption sample and the four Pu-doped magnetite samples), the Pu concentration remained below the detection limit of 10^{-9} M, hence an eventual effect of sorption or coprecipitation on Pu solubility cannot be derived.

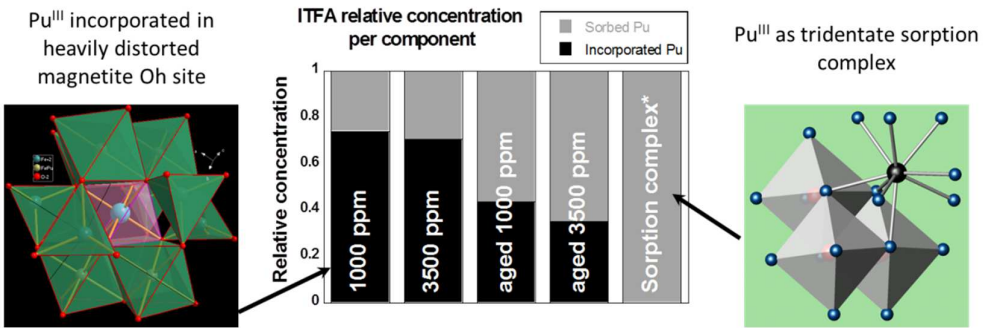

Figure 8: The two different Pu(III) endmember species (left and right) and their fractions in the magnetite samples before and after aging (center) as determined from the EXAFS spectra by ITFA.

2.1.2.2. Molecular mechanisms of Np reductive sorption and precipitation with siderite

The Np^{V} uptake by siderite during the sorption experiments is very high with log R_d values always above 5 and little variation across the pH range 7 to 13 (Figure 9, top). The addition of 0.1 M carbonate reduced Np uptake significantly between pH 8 and 11, i.e. in the pH region where siderite solubility is low. In comparison to the Np^{V} uptake by the (redox-inactive) Ca carbonate calcite, these log R_d values are two to three orders of magnitude higher, [44] and much more similar to values obtained for the tetravalent actinide, Th, on calcite, [45] in both cases at comparable pH. Hence the high log R_d values are a first indication that Np^{V} was reduced to Np^{IV} by siderite. Further support comes from by the thermodynamic calculation, showing that at the Eh values measured at pH 8, 10 and 12, the equilibrium should be dominated by NpO_2 (Figure 9, bottom).

Figure 10 shows the Np-L_{III} edge XANES spectra of the siderite sorption time series at pH 7.7 ±0.3, and of the coprecipitation sample. All spectra are well aligned and correspond both in edge and white-line position with the two Np^{IV} references, NpO_2 and the Np^{IV} aquo complex. [46, 47] This is further confirmed by the XANES edge energies as determined by the knot of the second derivative, which vary by less than 0.3 eV from the average of 17613.5 eV (Table 1). Furthermore, iterative transformation factor analysis performed with the software package ITFA on the XANES spectra revealed only one spectral component for the sorption samples, indicating that possible traces of Np^{V} remain below 5%. [43] Therefore, Np^{V} is reduced to Np^{IV} in all systems, even already after the shortest sorption time of 1 h, and also in the coprecipitation sample.

The EXAFS Fourier transform magnitudes of the sorption samples show a coordination shell at R+ΔR=1.8 Å (uncorrected for phase shift), which is fitted by about 8 oxygen atoms at a distance of 2.34 – 2.35 Å. Note that the small peak at the left side of this coordination shell cannot be fitted with a Np-O distance of 1.87 Å as would be expected for the –yl group of Np^{V}; they constitute instead a truncation artifact of the Fourier transformation arising from the relatively short k-range. A second peak at R+ΔR=3.7 Å increases in height with sorption time. Wavelet analysis of this peak reveals an amplitude maximum at k>10 $Å^{-1}$, in line with backscattering by a heavy element. [48] Correspondingly, this shell could be fitted with Np atoms at a distance of 3.82 – 3.84 Å

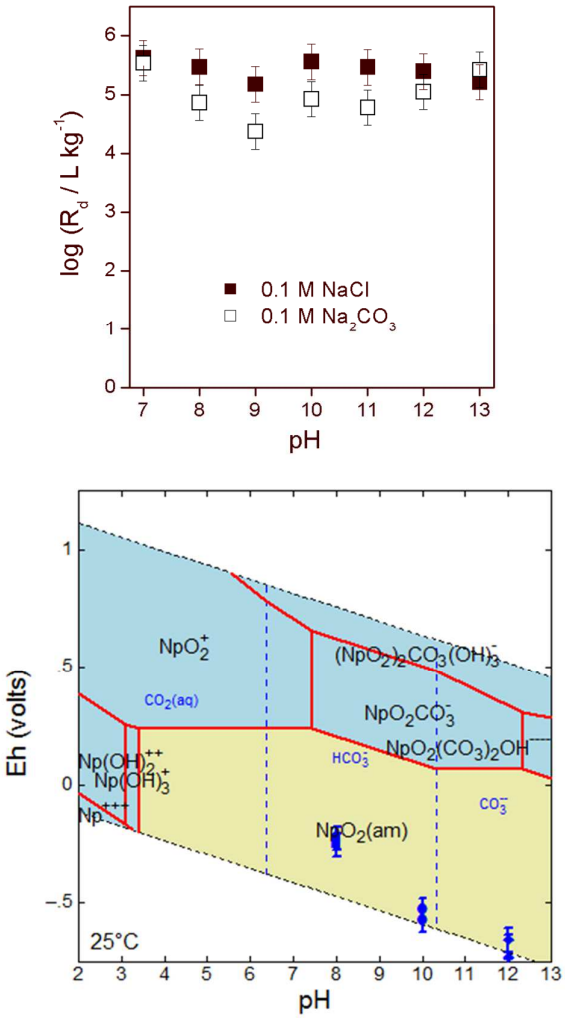

Figure 9: Top: Np solid/liquid distribution coefficient in the siderite system as function of pH. $[Np^{V}]_{ini}$ = 2·10^{-5} M, S/L = 1 g·L^{-1}, *I* = 0.1 M NaCl or $NaCO_3$ as indicated, after 1 week reaction time under anoxic N_2. Bottom: Eh-pH diagram calculated for the chemical system 2 10^{-5} M Np^{V} in 0.1 M NaCl solution in presence of siderite under anoxic conditions at 25°C (carbonate activity determined by siderite solubility). Thermodynamic data of the Lawrence Livermore National Laboratory *thermo* database were supplemented by the most recent NEA database. [49, 50] Results of batch experiments are represented by blue symbols.

The EXAFS Fourier transform magnitudes of the sorption samples show a coordination shell at R+ΔR=1.8 Å (uncorrected for phase shift), which is fitted by about 8 oxygen atoms at a distance of 2.34 – 2.35 Å. Note that the small peak at the left side of this coordination shell cannot be fitted with a Np-O distance of 1.87 Å as would be expected for the –yl group of Np^{V}; they constitute instead a truncation artifact of the Fourier transformation arising from the relatively short k-range. A second peak at R+ΔR=3.7 Å increases in height with sorption time. Wavelet analysis of this peak reveals an amplitude maximum at k>10 Å^{-1}, in line with backscattering by a heavy element. [48] Correspondingly, this shell could be fitted with Np atoms at a distance of 3.82 – 3.84 Å

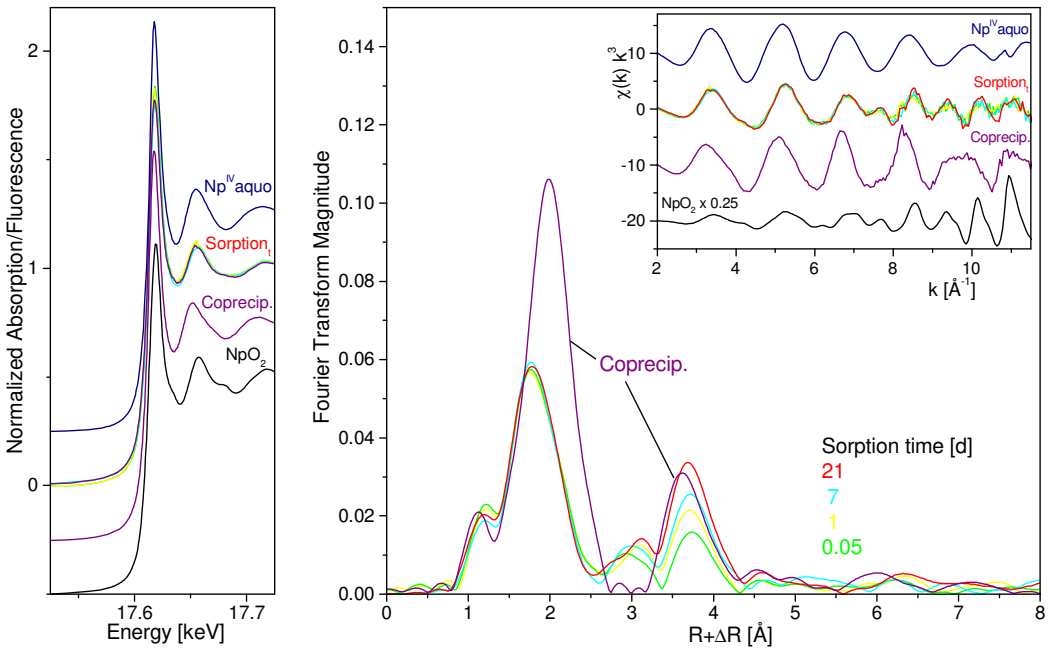

Figure 10: Neptunium L_{III}-edge XAS spectra of selected siderite sorption and coprecipitation samples (pH 7.7 ± 0.3) along with Np references. Left: XANES spectra, right: EXAFS Fourier transform magnitude and corresponding χ(k) spectra as insert.

Table 1. Np-L_{III} XANES edge energies and EXAFS fit results of Np siderite samples and references.

Sample	E_0 [eV]	First shell			Second shell				ΔE_0 [eV]	$\chi^2_{res\ \%}$
		CN[1]	R[2] [Å]	σ[2 3] [Å]	CN		R [Å]	σ [Å²]		
Sorp. 1 h (0.1 M)	17613.3	8.0 O	2.35	0.0100	2.1 Np		3.83	0.0026	7.1	19.3
Sorp. 1 d (0.1 M)	17613.4	7.7 O	2.35	0.0100	4.4 Np		3.84	0.0100	7.6	19.8
Sorp. 7 d (0.1 M)	17613.3	7.8 O	2.34	0.0100	3.9 Np		3.83	0.0054	7.4	16.4
Sorp. 21 d (0.1 M)	17613.5	7.9 O	2.34	0.0100	3.8 Np		3.82	0.0034	7.0	13.8
Sorp. 0.001 M (7 d)	17613.6	8.4 O	2.35	0.0100	3.4 Np		3.83	0.0027	7.4	14.6
Sorp. 1 M (7 d)	17613.6	8.0 O	2.34	0.0100	3.6 Np		3.83	0.0060	7.3	15.5
Coprecipitate	17613.8	9.6 O	2.41	0.0048	4.2	C_{bid}	2.87	0.0010	14.6	12.8
					4.2[c]	O_{dist}	4.14[c]	0.0016[c]		
					8.4[2c]	C_{bid}-O_{dist}	4.14[c]	0.0016[c]		
					4.2[c]	C_{bid}-O_{dist}-C_{bid}	4.14[c]	0.0016[c]		
Np^{IV}aquo	17613.8	11.6 O	2.39	0.0083					9.4	5.2
NpO_2	17613.6	8 O	2.35	0.0043	12	Np	3.85	0.0010	9.6	19.4
					24 O		4.48	0.0010		
NpO_2 crystal structure[51]		8 O	2.35		12	Np	3.84			
					24 O		4.51			

[1] CN: coordination number, error ± 25 %
[2] R: Radial distance, error ±0.01 Å
[3] σ2: Debye-Waller factor, error ±0.0005 Å²
[c] values correlated during fit

The interatomic distances (R) for these nearest Np–O and Np–Np shells are close to those of NpO_2 (Table 1). This is also true for the coordination numbers (CN) of the Np-O coordination shell, which are close to 8 as in the cubic NpO_2 structure. In contrast, the CNs of the Np-Np path are much lower, and their Debye–Waller factors (σ^2) as measure of static disorder much larger, than those of NpO_2, suggesting formation of nanoparticles. [51] Assuming NpO_2 particles with 1 nm diameter, one can calculate an average Np-Np coordination number of 5.5 (12×5+1×12) for such a cluster containing 13 Np atoms. This coordination number is significantly higher than the ones derived from the EXAFS shell fit (3.5 per average for all sorption samples), suggesting an even smaller average particle size, or cation vacancies. Similar trends were observed for nanocrystalline Np dioxide particles formed after dilution of aqueous Np^{IV} carbonate complexes [46] and for other An^{IV} oxide/hydroxide species. [18, 52, 53] Therefore, the EXAFS analysis suggests that Np^{V} reduction at the siderite surface leads to the formation of either small particles of crystalline NpO_2 or to structurally disordered Np^{IV} oxide/hydroxide. While the peak height of the Np-Np shell increases with increasing sorption time, suggesting the growth of nanoparticles with time, the shell fit data suggest a more complicated process: between 1 h and 1 d sorption time, the CN doubles from 2 to 4, but then remains constant. At the same time, the Debye-Waller factor increases from 0.0026 to 0.0100 $Å^2$, and decreases thereafter with increasing equilibration time to 0.0034 $Å^2$. This suggests that the initial particles are small, but well ordered, and then grow with high disorder, which subsequently obtain a higher degree of order with equilibration time. Ionic strength of the background electrolyte also shows a significant effect on the Debye-Waller factor, which increases from 0.0027 to 0.0054 to 0.0060 $Å^2$, when the ionic strength increases from 0.001 to 0.1 to 1 M for a constant reaction time of 7 d. Therefore, increasing background electrolyte concentrations increasingly interferes with the crystallization process.

To further characterize the microstructure of the Np^{IV} phase, a dried Np siderite suspension was analyzed using TEM. A typical bright-field TEM micrograph is shown in Figure 11 a. While the black particle with a diameter of approximately 40 nm is siderite, the gray areas arise from particles much smaller. The HRTEM micrograph (Figure 11 b) shows periodic structures with diameters ≤ 1-2 nm (marked by circles). The diffractogram based on Fast Fourier Transform (FFT) analysis of the HRTEM image consists of diffuse rings as expected for such nanocrystalline material, which are not accessible to structure analysis. However, the dominant presence of Np and O determined in an adjacent region by energy-dispersive X-ray (EDX) spectroscopy (Figure 11 c) confirms that these small particles constitute indeed the Np phase (Note that C and Cu contributions stem from the TEM support grid, and Fe and Co from the objective lens pole piece). Extended electron irradiation (1-2 min.) induced particle growth, and the FFT-derived diffraction pattern of those irradiated regions produced now distinctive diffraction rings in agreement with the fluorite-type NpO_2 structure ($Fm\bar{3}m$) (Figure 12). [54] Thus, the TEM-derived particle size of the unaltered material and the phase identification after the electron-induced particle growth support the EXAFS analysis that Np^{IV} is precipitated as NpO_2 or a hydrated precursor phase with particle sizes around 1 nm or even smaller.

In contrast to the sorption samples, the EXAFS Fourier transform magnitude of the coprecipitation sample shows a much higher and more distant coordination shell (Figure 10 right), which could be fitted with ~10 oxygen atoms at a distance of 2.41 Å, *i.e.* not commensurate to the cubic NpO_2 structure (Table 1). Furthermore, the second shell is at a shorter distance than the Np-Np shell of NpO_2. Wavelet analysis of this shell shows a maximum of k at about 8 $Å^{-1}$, and hence discards that this peak arises from Np-Np backscattering. The spectrum is in fact similar to compounds where carbon is bidentately coordinated, like in Ce^{IV} or U^{IV} carbonate compounds. [55] This was confirmed by a shell fit based on this bidentate arrangement, which gives rise to very characteristic multiple scattering paths involving the nearest bidentately coordinated C ($C_{bid)}$ and the next nearest, distal O (O_{dist}) atom of the carbonate molecule. The Np-O coordination number of ~10 as well as the Np-C_{bid} coordination number of 4.2 (theoretically 5) confirm the formation of $Np^{IV}(CO_3)_5$ units very similar to those found for U^{IV} and Pu^{IV} before, in line with the similar complex formation constants of all three actinides. [50, 55, 56] As expected for the slightly smaller ionic radius of Np^{IV} versus U^{IV}, the fitted radial distances are about 0.02 Å shorter

than for the U^{IV} carbonate unit (Table 1). Analogous to U^{IV}, the Np^{IV} pentacarbonate unit may exist either as aquo-anion complex, [46] or in the solid state with *e.g.* Na for charge compensation and crystal water. [55] The relatively strong association of this Np^{IV} species with the solid phase (log R_d = 4.0) leaves little doubt about the solid-state nature of this Np^{IV} carbonate species, since the potentially 6-fold negative charge of the aquo-anion would prevent strong sorption to the siderite surface. Furthermore, a fit of the spectrum assuming that Np^{IV} resides in the octahedrally coordinated position of Fe^{II} in siderite failed due to the fact that no Np-C shell at a distance of 3.0 to 3.4 Å could be fitted, which would be characteristic for the monodentate coordination of carbon and the cations in siderite. Therefore, our results demonstrate that Np^{IV} does not form part of the siderite structure through co-precipitation, but is entrapped by formation of a Np^{IV} carbonate precipitate. Evidently, the strong complexation of Np with dissolved carbonate prevented the incorporation by siderite. [50]

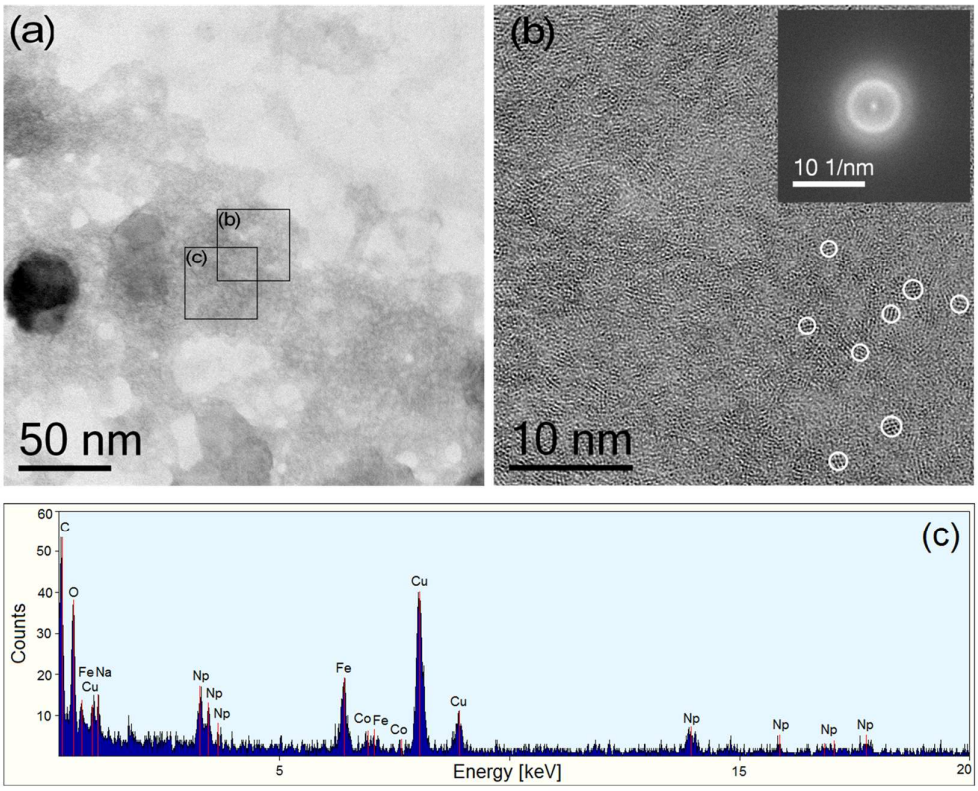

Figure 11: (a) Bright-field TEM micrograph of a dried Np siderite suspension ($[Np^V]_{ini}$ = $2 \cdot 10^{-5}$ M, S/L = 0.1 $g \cdot L^{-1}$, pH=7.6, I = 0.1 M (NaCl), after 7 d under anoxic conditions). (b) HRTEM image of area (b) with corresponding Fast Fourier Transform (FFT) in the inset. Some nanocrystals are marked by circles. (c) Energy-dispersive X-ray (EDX) spectrum obtained in scanning TEM mode from the area (c).

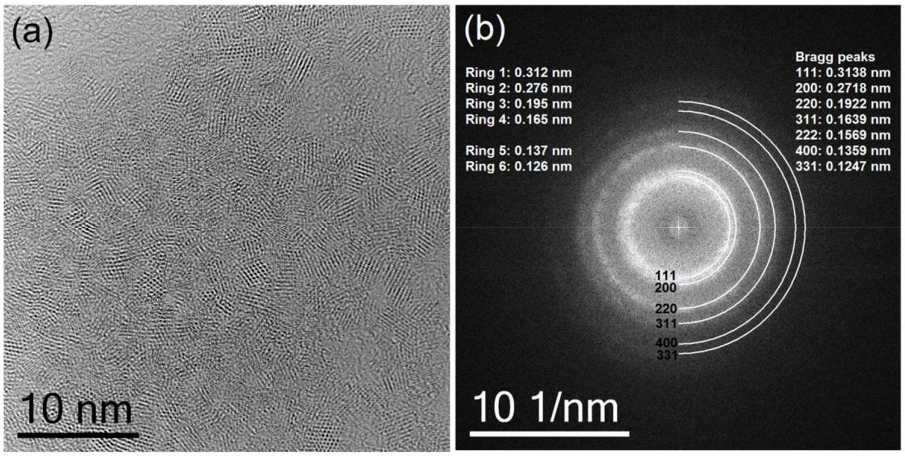

Figure 12: (a) HRTEM image of the same 7-d sorption sample as in **Figure 11**, but after extended electron irradiation (1-2 min.) and (b) corresponding diffractogram derived from FFT analysis of (a).

After reaction of Np^{V} with siderite in the pH range 7-8 most relevant for siderite-containing clay rocks, [57] we could demonstrate for the first time the formation of NpO_2-like nanoparticles. The formation of a NpO_2-like phase by a surface-mediated redox reaction is in line with results by a recent study showing Np^{V} reduction by biotite and chlorite with reduced structural iron. [41] It is also in line with formation of UO_2–like nanoparticles upon U^{VI} sorption to *e.g.* magnetite and mackinawite. [58, 59] Formation of monomeric Np^{IV} sorption complexes was not observed at the given reaction conditions, but may form when initial Np concentrations remain below the solubility of NpO_2(am). Interestingly, the strong affinity of Np^{IV} towards carbonate did not prevent the precipitation of the NpO_2-like phase, likewise to the formation of PuO_2 after reaction of Pu^{V} with the Fe^{II} hydroxocarbonate chukanovite. [11] This can be explained by the relatively low siderite solubility in the investigated pH range. Only during coprecipitation (*i.e.* when Np^{V} was added to the 0.8 M carbonate solution prior to siderite precipitation), strong carbonate complexation and subsequent precipitation of a Np^{IV} pentacarbonate took place. Since such high carbonate concentrations are not to be expected under radioactive waste conditions, formation of NpO_2-like nanoparticles is certainly more relevant for the safety case.

For equilibration periods up to one day, the measured equilibrium concentrations of Np were found to be two orders of magnitude larger than those expected in equilibrium with NpO_2(am) ([Np] = 10^{-9} M). [50] This effect is explained by formation of colloidal NpO_2(am) in agreement with other amorphous actinide(IV) oxyhydroxide colloids. [60] After 7 days of equilibration, however, the Np concentrations decreased almost to the value of NpO_2(am). Interestingly, this lower solubility coincides with a higher static order as reflected by lower Debye-Waller factor of the Np-Np paths as compared to the 1 day sample (Table 1). Even addition of a high concentration of carbonate (0.1 M) had only a relatively small influence on Np retention, in line with previous results. [61, 62]

The observed high retention of Np by siderite across a relatively wide pH range is encouraging. However, the potential mobilization of the formed NpO_2–like nanoparticles as colloids may significantly raise the risk of Np migration away from the waste disposal site. [63, 64] In case of the redox sensitive uranium, the two-electron transition from U^{VI} to U^{IV} requires the formation of a chemical bond with an electron-donor surface, while the formation of aqueous Fe-U ion pairs can provide only one electron, thereby hindering the redox reaction kinetically. [65] Not surprizing, TEM images of surface-catalyzed UO_2 show an intimate spatial association with the most reactive sites on mineral surfaces. [58, 59] This is not the case for the NpO_2 particles, which are diffusely distributed between the siderite particles (Figure 11 a), thereby suggesting that the single electron required for the Np^{V} reduction might be provided

by dissolved Fe^{II} species. This is further supported by the high isoelectric point of siderite (pH 10.1), leading to charge repulsion between the (net) positively charged siderite surface and the cationic $Np^{V}O_2^+$ species prevailing below pH 10, which should also favor the redox reaction between dissolved Np^{V} and Fe^{II} species. Therefore, the NpO_2–like nanoparticles formed in presence of siderite may have a significant tendency to become detached from the mineral assembly. This does not necessarily mean that they also have a strong tendency to form mobile colloids, since their surface charge is low at circumneutral conditions, which favors their coagulation and causes a relatively fast settling. [46] This, however, may change in the presence of dissolved silica, since then amorphous NpO_2 silica structures can form, whose negatively-charged silanol surface groups may provide rather stable colloidal suspensions. [66]

2.1.2.3. Molecular mechanisms of Np reductive sorption and precipitation with magnetite

Figure 13 (left) shows the Np L_{III} XANES spectra of 12 Np^{V} magnetite sorption samples at three different pH values (6, 8 and 12) and after four different equilibration times (1 hour, 1 day, 1 week, 3 weeks). A comparison with Np^{IV} (blue) and Np^{V} (red) standards demonstrates, that all sorption samples (black) contain prevalently Np^{IV}. Statistical analysis with ITFA showed furthermore, that all samples contain less than 5 % of Np^{V}. The corresponding 12 EXAFS spectra (Figure 13 center and right) can be reconstructed by only two principal components, i.e. all samples contain only two different Np species. Based on VARIMAX rotation, the first spectrum at pH 6 and 1 h reaction time represents the first endmember species, and the last spectrum at pH 12 and 3 weeks reaction time represents the second endmember species. The first spectral species could be fitted with a nine-fold Np-O coordination sphere in the typical tricapped prismatic configuration, where the 3 oxygen atoms in the equatorial plane have a shorter distance from Np than the 6 oxygen atoms pointing upward and downward (Table 2). The fit is complemented by 3 Fe atoms 3.45 Å, in line with a tridentate sorption complex. This sorption complex is similar to the one found for Pu^{III} at the {111} faces of magnetite. The fit of the second spectral species reveals the formation of NpO_2-like nanoparticles similar to the Np species found in the Np/siderite system.

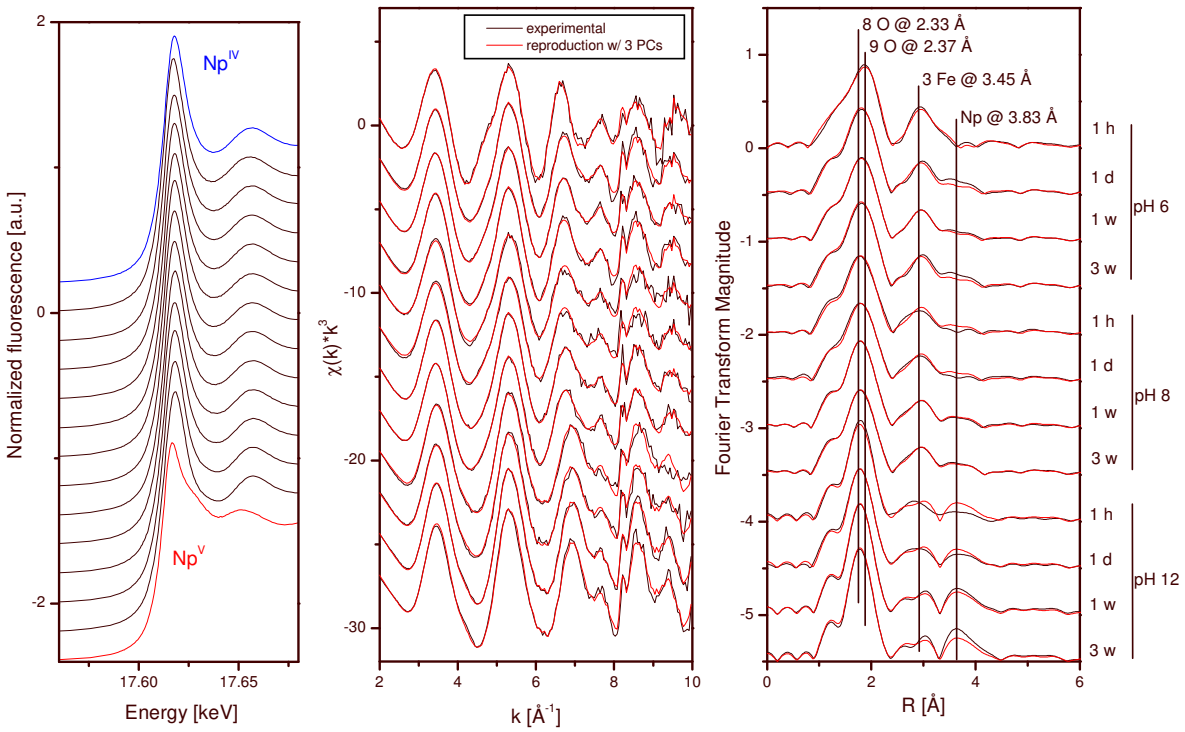

Figure 13: Np L_{III} XANES and EXAFS spectra of Np sorbed magnetite samples at three different pH values and four different equilibration times as indicated in the figure. All 12 experimental EXAFS spectra (black traces) could be reconstructed with two components (red traces).

The quantification of the two species based on iterative target test transformation of the 12 EXAFS spectra shows again that the tridentate sorption complex occurs in pure form only after the shortest reaction time at pH 6, while the longer reaction times lead to a 2/1 mixture of the sorption complex and the NpO_2 nanoparticles (Figure 14). This mixture is also present for all samples at pH 8 (spectra # 5 to 8). At pH 12, however, the NpO_2 nanoparticles prevail at all equilibration steps.

Figure 15 shows the measured Eh and pH values of the samples (blue markers) plotted into Pourbaix diagrams of Np (left) and Fe (right) speciation. According to these thermodynamic calculations, one would expect that all Np^{IV} occurs as NpO_2 only. Therefore, formation of the tridentate sorption complex effectively competes with precipitation of NpO_2 in the pH range 6 to 8, suggesting a high bond strength and associated low solubility of this sorption complex. A similar mechanism may have led to the formation of mononuclear U^{IV} sorption complexes previously observed on mineral and bacterial surfaces. Likewise to Pu^{III}, magnetite as e^- conducting and O-terminated mineral phase shows a strong tendency to keep reduced Np^{IV} as a sorption complex, while structural incorporation was not observed, neither for the longterm sorption samples nor for a coprecipitation sample, where Np^{V} remained in its original oxidation state as (weak) sorption complex (not shown).

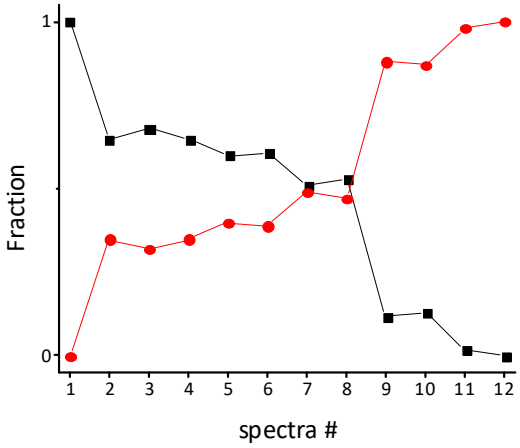

Figure 14: Fraction of Np species 1 (black) and Np species 2 (red) in the 12 sorption samples shown in Figure 13 from top to bottom.

Table 2. Shell fit of the two endmember spectra derived by ITFA from the 12 EXAFS spectra (Figure 13).

Sample	E/eV*	Path	CN†	R/Å	σ^2/Å^2	ΔE^0/eV	%R‡
PC1	17,613.0	Np-O1	3[f]	2.25	0.0032	8.1	7.8
(pH 6, 1 h)		Np-O2	6[f]	2.43	0.0052		
		Np-Fe	3[f]	3.45	0.0071		
PC2	17,613.1	Np-O	8[f]	2.33	0.0096	9.1	9.9
(pH 12, 3 wk)		Np-Np	3.5	3.83	0.0043		

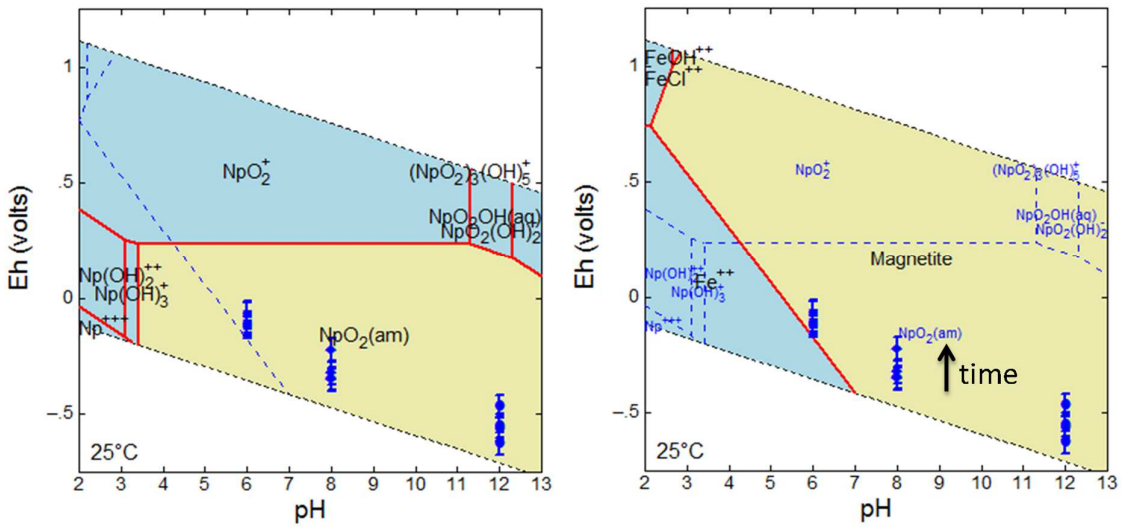

Figure 15. Pourbaix diagrams showing the pH/Eh dependence of Np (left) and Fe species (right), along with the measured pH and Eh values at the three different pH values (blue markers; note the effect of increasing equilibration time indicated by the black arrow).

2.1.2.4. Molecular mechanisms of Np reductive sorption and precipitation with mackinawite

The Np L_{III} XANES and EXAFS spectra of the Np mackinawite sorption samples and of one coprecipitation sample are shown in Figure 16. The XANES spectra are in line with a complete reduction of Np^{V} to Np^{IV} for the sorption samples. This is further confirmed by the coordination shell, which could be fitted with 9 O atoms at a distance of 2.37 Å. No additional S coordination shell could be fitted, in disagreement with the work of Moyes et al. who observed a partial coordination to S. [38] Furthermore, the spectra show a relatively weak Np-Np backscattering peak in line with formation of a nanoparticulate NpO_2-like phase, but also a weak contribution from an Np-Fe path. Neptunium in this samples hence occurs as both nanoparticles and a sorption complex. Ongoing further analysis is required to fully elucidate the speciation. The coprecipitation sample shows predominant Np reduction and (partial) incorporation into an unidentified Fe oxide. As for the sorption samples, further analyses are necessary to elucidate the Np speciation in this sample. In conclusion, mackinawite, which is e^- conducting, but in contrast to magnetite S-terminated, is less reactive for "hard" actinides, in contrast to the fission products Se and Tc.

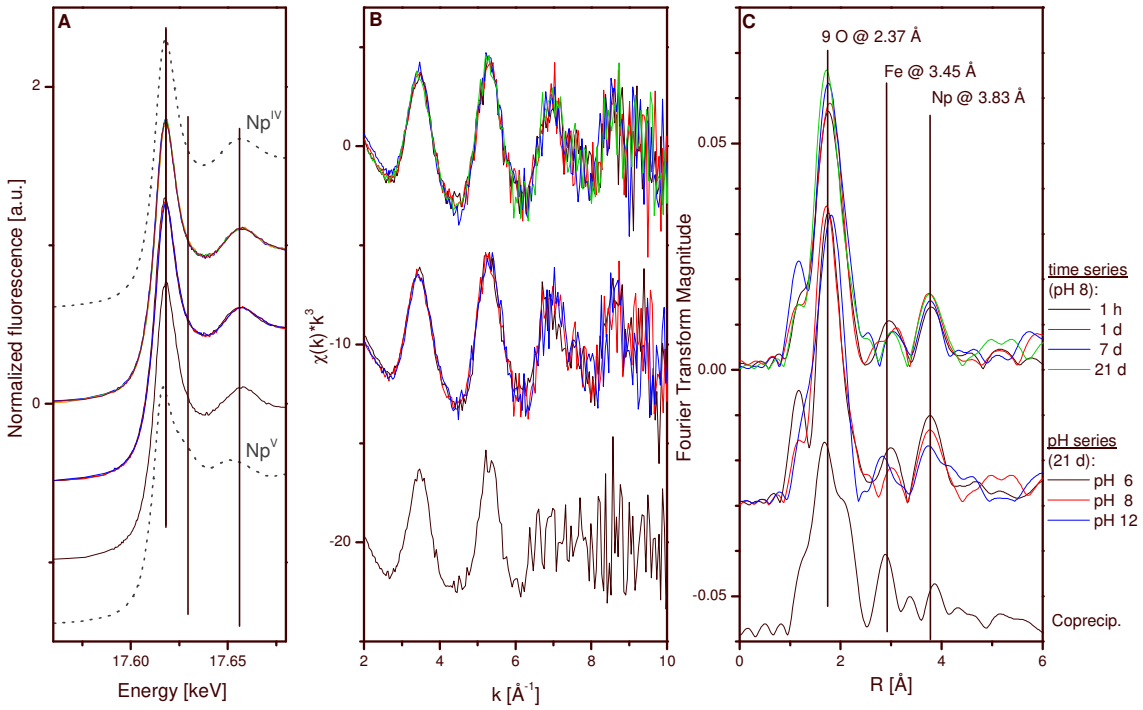

Figure 16: Np L_{III} XANES and EXAFS spectra of Np sorbed mackinawite samples as time series at pH 8, and as pH series after 21 days of reaction time. The spectrum of a coprecipitation samples is shown in black at the bottom.

2.1.2.5 Molecular mechanisms of Se reductive sorption and precipitation in cement systems

In collaboration with PSI-LES, X-ray absorption spectroscopy experiments were conducted and the obtained spectral data analysed to elucidate the chemical state of Se(-II) in cement systems. XAS investigations were performed on two types of AFm phases loaded with HSe^-: an AFm-phase with a low affinity for HSe-: AFm-CO_3 and an AFm-phase with a high affinity for HSe-: AFm-$OHCO_3$. The equilibration time in these experiments was 1 month. The Se loading varied between ~ $6{\cdot}10^{-3}$ mol kg^{-1} (500 ppm) and $4{\cdot}10^{-2}$ mol kg^{-1} (3000 ppm). The equilibrium aqueous Se concentrations in these experiments were $5{\cdot}10^{-5}$ M < $[Se]_{eq}$ < $2{\cdot}10^{-4}$ M in the case of the experiments with AFm-CO_3 and < 10^{-5} M in the case of the experiments with AFm-$OHCO_3$. The Se redox speciation in these supernatant solutions was not measured, but, based upon the insights obtained from the macroscopic experiments in the previous

section, it can be assumed that after 1 month equilibration, in the experiments with AFm-CO_3 the majority of the aqueous Se still was present as HSe^- whereas in the experiments with AFm-$OHCO_3$ the majority of the aqueous Se was oxidized.

Figure 17 shows the XAFS spectra of HSe^- sorbed onto MC1500 (AFm-CO_3 phase) and onto HC1500 (AFm-$OHCO_3$ phase) as red traces, in comparison to the spectra of red Se(0) and the HSe^- aquo complex (gray traces). The XANES spectra of MC1500, HC1500 and HSe^- all show a similar white line position, which is at higher energy than the white line position of Se(0). While this would suggest a Se oxidation state higher than 0 at first glance, a comparison of references shown in the same figure and previous publications [9, 67] reveal a sharp white-line feature for Fe selenides at about the same energy or even slightly below that of Se(0). This feature is also clearly present in the onset of the XANES edges of MC and HC, and to a lesser degree in the onset of the XANES of HSe^-. Its left-wing inflexion reveals an edge energy of 12650 eV (Table 3), about 5 eV below the edge energy of Se(0) compounds, thereby confirming a (-II) oxidation state of the Se sorbed on both AFm phases notwithstanding the higher oxidation state of Se in the supernatant solutions. HSe^- sorption onto both AFm phases thus appears to stabilize the (-II) oxidation state.

The Fourier Transform Magnitudes of the XAFS spectra of Se(-II) in HSe^-, AFm-CO_3 and AFm-$OHCO_3$ show a coordination peak at about 2.8 Å (no phase shift correction). The corresponding k^3-weighted chi-spectra show that the main frequency has an amplitude maximum at a low k-value of about 3 $Å^{-1}$, which is typical for low-z elements like O. In contrast, Se compounds with Se and/or Fe next neighbours have an amplitude maximum at much higher k-values, as revealed by the chi-spectrum of red Se(0). A first guess was therefore, that Se(-II) in HSe^-, AFm-CO_3 and AFm-$OHCO_3$ is surrounded by water molecules at a relatively long distance. In a reference structure, the highly hydrated Se(-II) compound Na_2Se nonahydrate, Se(-II) is surrounded by 12 water molecules, with Se-O distances between 3.31 and 3.56 Å.[68] Using this structure to calculate theoretical backscattering paths with FEFF8.2 and applying XAFS shell fitting, we obtained for HSe^- a similar coordination environment with about 12 O atoms at an average distance of 3.36 Å (Table 3). The relatively high Debye-Waller factor of 0.0106 $Å^2$, determined at a temperature of about 15 K where thermal contributions are negligible, is in line with a relatively wide distribution of Se-water distances similar to the solid Na_2Se nonahydrate. No statistically significant paths beyond this first water shell could be fitted for HSe^-.

This is different for MC1500 and HC1500 samples: their Fourier Transform Magnitudes show not only a strong peak at about 2.8 Å, but also additional peaks at 4.7 and 6.8 Å, suggesting structural order beyond the first coordination sphere. At least for HC1500 with its larger d-spacing of 8.20 Å and the high HSe^- loadings, HSe^- sorption may proceed at least partially through the replacement of the $[OH(CO_3^{2-})0.5]^{2-}$ anions in the interlayer space. Given the same charge and a similar ionic radius of Cl^- and HSe^-, HSe^- is likely to adopt a similar local coordination as Cl^- in AFm-Cl_2 (Figure 18).[69] At this 3(b) site of the rhombohedral R-3 space group, Cl- sits on top of a 7-coordinated Ca polyhedron (blue), which is surrounded by three other 7-coordinated Ca polyhedra (blue) and three Al octahedra (red). Bonding takes place through 3 OH groups (light blue balls), which are each triply coordinated to two Ca polyhedra and one Al octahedron, and through 3 H_2O groups (purple balls), which form the apical corners of the Ca polyhedra protruding into the interlayer space. Since Cl^- in the interlayer binds to the double-hydroxide layers on both sides in exactly the same way, Cl^- is coordinated in total to 3 O atoms at 3.41 Å (H_2O), to 3 O atoms at 3.45 Å (OH groups), to 2 Ca atoms at 4.51 Å (axial Ca atoms directly above and below), to 6 Ca atoms at 4.70 Å, and to 6 Al atoms at 5.13 Å (Table 1).We replaced Cl by Se and calculated the theoretical XAFS paths with FEFF8.2. Fitting this model to the HC1500 spectrum required only two constraints to obtain a statistically reliable fit with physically consistent parameters: (1) A preliminary fit of the first FTM peak showed that two different Se-O paths are required to fit the split first FTM peak, although the distal differences in the original Cl model are below the XAFS resolution ($\pi/(k_{max}-k_{min})/2=0.14$ Å). The coordination numbers of both paths were close to 6 and were therefore fixed to 6 for the subsequent fits. (2) The coordination numbers of the longer Se-Ca path and the Se-Al path were kept correlated to account for the characteristic structure of the double-hydroxide

layers. The resulting fit parameters are given in Table 3 along with the starting values of the hydrocalumite-based model.

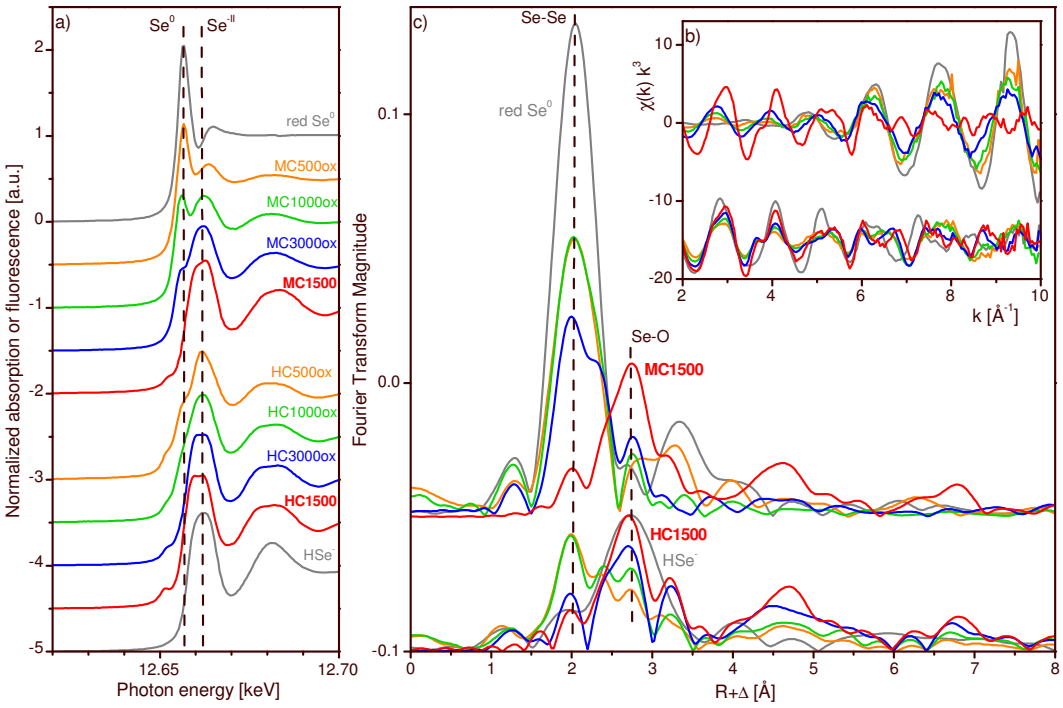

Figure 17: Se-K edge XAS spectra of Se-sorbed monocarbonate (MC (AFm-CO_3), red top) and hemicarbonate (HC (AFm-$OHCO_3$), red bottom) along with their respective oxidation series (blue->green->orange). The spectra of red Se(0) and of HSe^- are shown in gray. XANES (left), EXAFS Fourier Transform Magnitude (right) and k_3-weighted χ(k) spectra (insert).

Table 3: Se-K XANES edge energies and EXAFS fit results of AFm samples and selected references. Crystallographic values of hydrocalumite as reference for HSe^- in HC1500,[69] of Na2Se 9H2O as reference for the HSe^- aquo complex,[68] and of red Se [70] are given in brackets.

Sample	E_0 [eV]	Coordination shell			Further shells			ΔE_0 [eV]	$\chi^2_{res\ \%}$
		CN	R [Å]	σ^2 [Å²]	CN	R [Å]	σ^2 [Å²]		
HC1500	12650.3	6^{f}O	3.28 (3.41)	0.0047	2.0Ca (2)	4.41 (4.51)	0.0121	4.1	19.0
		6^{f}O	3.49 (3.45)	0.0062	6.8^{c}Ca (6)	4.65 (4.70)	0.0150		
					6.8^{c}Al (6)	5.27 (5.13)	0.0070		
MC1500	12650.4	6^{f}O	3.25	0.0052	0.6Ca	4.38	0.0120	3.5	18.1
		6^f O	3.43	0.0065	4.8^{c}Ca	4.60	0.0128		
					4.8^c Al	5.21	0.0059		
HSe^-_{aquo}	12650.5	12.4O (12)	3.36 (3.31-3.56)	0.0106				3.1	11.7
red Se^0	12655.6	2 Se	2.36 (2.33)	0.0026	4.9Se (5)	3.73 (3.66-3.82)	0.0076	13.5	17.7
					4.1Se (4)	3.92 (3.83-3.99)	0.0100		

CN: coordination number with error ± 25 %, R: Radial distance with error ±0.01 Å, σ^2: Debye-Waller factor with error ±0.0005 Å², f: values fixed during fit, c: value correlated during fit.

The Se-Ca and Se-Al coordination numbers are (within errors of ±25%) as expected for HSe^- in the interlayer space and bonding to both double-hydroxide layers. The first Se-Ca path is 2% shorter, the second Se-Ca path is 1% shorter, and the Se-Al path is 3% longer compared to the (very symmetrical) Cl position in AFm-Cl_2. This are relatively small deviations, which can be explained by a higher structural disorder of Se(-II) in AFm-$OHCO_3$, which is also in line with the relatively high Debye-Waller factors. Furthermore, the two Se-O shells are split by 0.21 Å, also indicating a more distorted local coordination of HSe^- bonding to the two layers. Despite the modest distortion of the local environment, coordination numbers and distances are fully in line with HSe^- sorbed in the interlayer space of AFm-$OHCO_3$.

While the XAFS spectra of HC1500 and MC1500 samples appear quite similar, the shell fit using the same procedure as described above produced small, but statistically significant differences. While the Se-O coordination is again split in two subshells with 6 oxygen atoms each, the average distance of both shells is 3.34 Å and hence 0.05 Å smaller than for HC1500. The distances of the following Ca and Al shells are also slightly smaller (0.03, 0.05 and 0.06 Å), showing a consistent contraction of the Se environment by about 1%. Furthermore, the coordination numbers of the Se-metal shells are consistently smaller (0.6 for the short Se-Ca path and 4.8 for the longer Se-Ca and Se-Al paths). These smaller coordination numbers suggest that a substantial part of HSe^- is bound to the outside surfaces of the AFm-CO_3 phase, forming a similar sorption complex as in the interlayer space, but with bonds to only one side. This is in line with the AFm-CO_3 structure in which CO_3^{2-} anions are strongly retained in the AFm-CO_3 interlayer by a direct bond with Ca ions from the main layer, thus hindering the penetration of HSe^-. If we assume that HSe^- binds exclusively to the outside surface, however, coordination numbers of 1 for the short Se-Ca path and 3 for the subsequent Se-Ca and Se-Al paths would be expected. The observed CN of 4.8 is 60% higher, hence above the error limit of 25%. Therefore, HSe^- does not seem to reside exclusively at the outer surfaces, but also partly in the interlayer space. Given the relatively errors, we did not attempt to estimate the ratio of Se in the interlayers vs. on outer surfaces from the coordination numbers. The 1% contraction of the local environment could either arise from the fact that HSe^- needs to adapt to the surface atoms of only one side, but could also arise from the smaller interlayer space of AFm-CO_3, hence cannot be used to quantify the distribution between both sites.

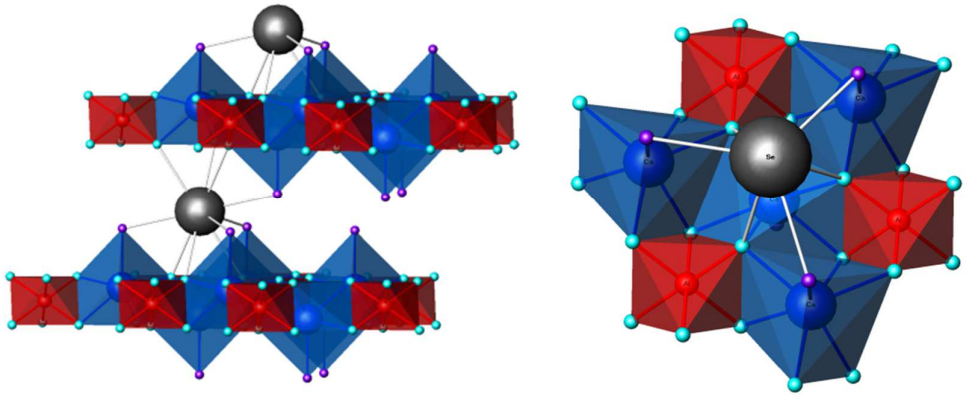

Figure 18: Hydrocalumite-based structural model of the EXAFS-derived positions of Se (gray balls) in AFm-CO_3 and AFm-$OHCO_3$ (left : side view left, right : top view). HSe^- attaches to the surface Ca/Al double hydroxide layers through three OH-oxygen (light blue balls) and three H_2O-oxygen atoms (purple balls), forming edge-sharing complexes with four $Ca(OH)_7$ polyhedra (blue) and corner sharing complexes with 3 $Al(OH)_6$ octahedra (red) (right and top left). In the interlayer space, this coordination geometry is doubled since HSe^- is able to bind to the two adjacent layers in the same way (center left).

Further support that a substantial fraction of Se(-II) is sorbed to the outer layers comes from the XAS spectra of a controlled oxidation experiment in which AFm samples loaded with increasing amounts of Se(-II) (500 ppm, 1000 ppm and 3000 ppm) were exposed to air for a short time (10 minutes) (Figure

17). The XANES spectrum of MC3000ox shows a shoulder at the white position of Se(0), which grows into a distinct Se(0) white line with decreasing Se concentration (MC1000ox and MC500ox). The increasing formation of Se(0) with decreasing Se concentration is also shown by the XAFS chi spectra, which show an increasing amplitude of the oscillations at high k-range, and by the corresponding FTM with an increasing peak at about 2 Å in line with that of red Se(0) shown for comparison. Factor analysis coupled to an iterative target test [43, 71] using the spectra of MC1500 and red Se(0) as pure endmembers showed that samples MC3000ox, MC1000ox and MC500ox contain about 50, 70 and 80% of Se(0), respectively. This tendency is much less expressed by the corresponding AFm-$OHCO_3$ series as is evident from the XANES and XAFS spectra, as well as from the iterative target test (5, 25 and 30% of Se(0) for samples HC3000ox, HC1000ox and HC500ox, respectively). Since Se(-II) present in the interlayer space at high loadings is better protected from oxidation than Se(-II) at the outer surfaces, this difference in degree of oxidation supports the structural interpretation of the non-oxidized endmember spectra of AFm-$OHCO_3$ and AFm-CO_3, that HSe^- in AFm-$OHCO_3$ sorbs prevalently in the interlayer space, while AFm-CO_3 has a higher degree of sorption to the surface sites because of restricted access to the interlayer space.

2.1.2.6 Uptake of Se during the ferrihydrite-hematite recrystallization

In collaboration with KIT-IMG, X-ray absorption spectroscopy experiments were conducted and the obtained spectral data analysed to elucidate the chemical state of Se during the ferrihydrite hematite recrystallization. Comparative adsorption studies, performed at identical conditions, allowed a distinction between pure adsorption and coprecipitation and showed a significantly higher Se retention by coprecipitation than by adsorption. Desorption studies indicated that Se coprecipitation leads to the occurrence of a resistant, non-desorbable Se fraction. According to time-resolved studies of Se(IV) or Se(VI) retention during the hematite formation and detailed spectroscopic analyses (XPS, XAS), this fraction is the result of an incorporation process, which is not attributable to Fe-for-Se substitution or the Se occupation of vacancies. Se initially adsorbs to the ferrihydrite surface, but after the transformation of ferrihydrite into hematite, it is mostly incorporated by hematite. In systems without mineral transformation, however, Se remains as a sorption complex. In case of Se(VI), an outer-sphere complex forms, while Se(IV) forms a mixture of bidentate mononuclear edge-sharing and bidentate binuclear corner-sharing inner-sphere complexes. The results of this study demonstrate that occlusion of Se oxyanions by hematite is an important retention mechanism, in addition to pure adsorption, for immobilizing Se in natural systems, which may control Se migration processes in polluted environments.

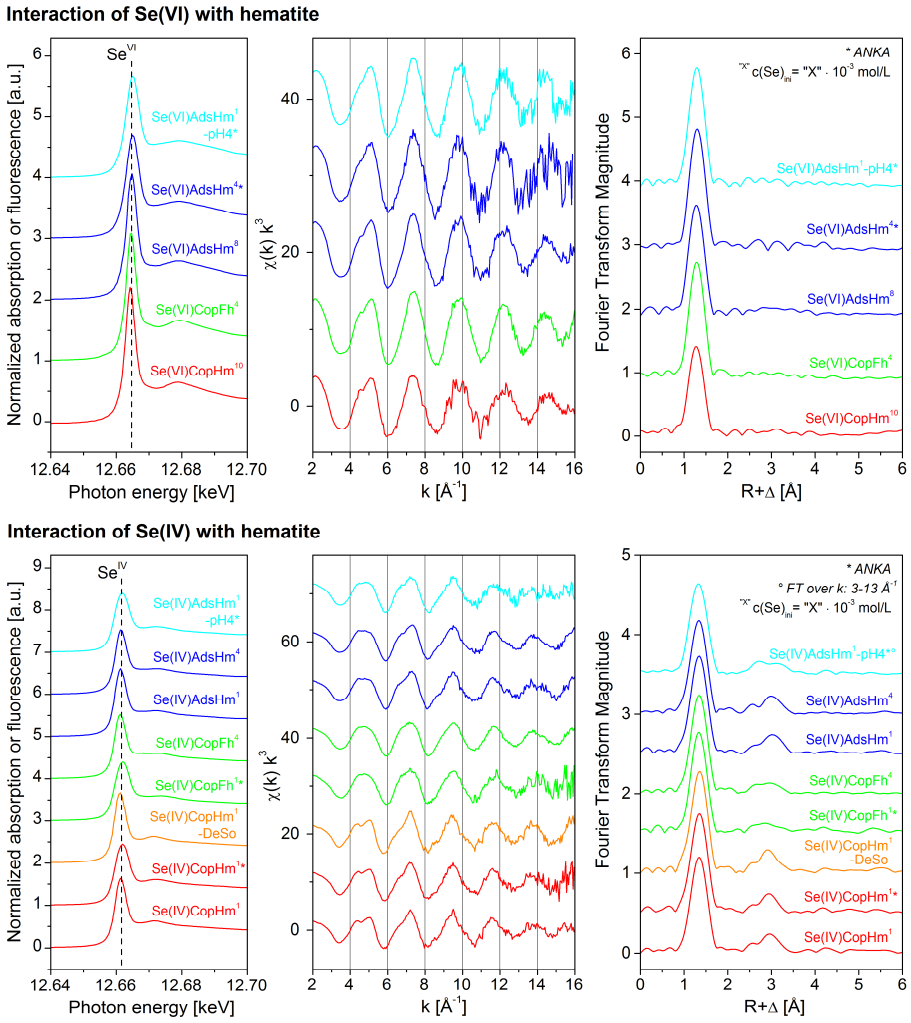

Figure 19: Se K-edge XANES and EXAFS spectra of Se(IV) and Se(VI) bearing hematite (Hm) and ferrihydrite (Fh) samples of different coprecipitation (Cop) and adsorption (Ads) studies. (If not otherwise indicated, EXAFS Fourier transforms (FT) were calculated over the k-range 3-14.5 Å^{-1})

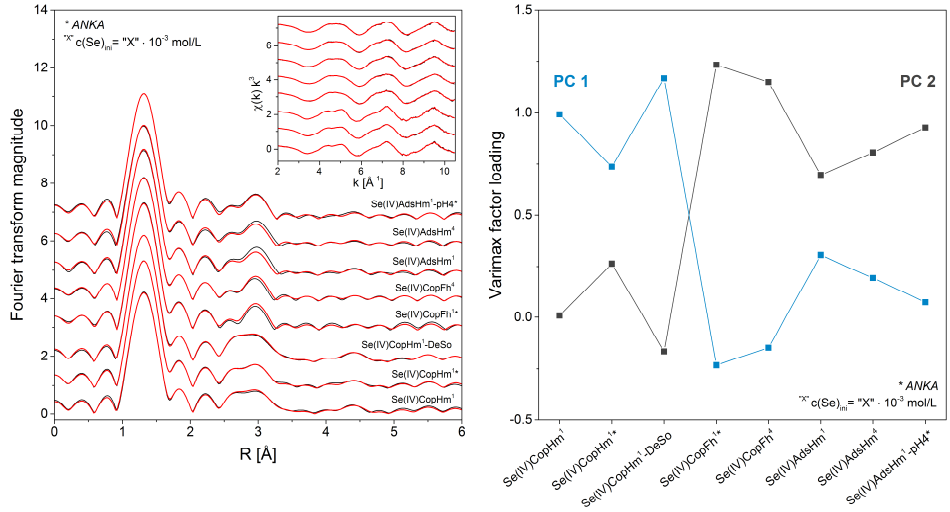

Figure 20. Iterative transformation factor analysis of Se K-edge EXAFS spectra. Left: Experimental FT spectra (black lines) and their reconstruction (red lines) by two principal components (PC). EXAFS Fourier transforms were calculated over the k-range 2-10.5 Å^{-1}. Right: Varimax loadings of the spectral components.

2.1.2.7. Literaturverzeichnis

(1) Sellin, P.; Leupin, O. X. The use of clay as an engineered barrier in radioactive waste management - A review. *Clays and Clay Minerals* **2013,** *61* (6), 477-498.

(2) Schlegel, M. L.; Bataillon, C.; Blanc, C.; Pret, D.; Foy, E. Anodic activation of iron corrosion in clay media under water-saturated conditions at 90 degrees C: Characterization of the corrosion interface. *Environmental Science & Technology* **2010,** *44* (4), 1503-1508.

(3) Wersin, P.; Jenni, A.; Mader, U. K. Interaction of corroding iron with bentonite in the ABM1 experiment at Aspo, Sweden: A microscopic approach. *Clays and Clay Minerals* **2015,** *63* (1-2), 51-68.

(4) Grambow, B.; Smailos, E.; Geckeis, H.; Muller, R.; Hentschel, H. Sorption and reduction of uranium(VI) on iron corrosion products under reducing saline conditions. *Radiochimica Acta* **1996,** *74*, 149-154.

(5) El Hajj, H.; Abdelouas, A.; El Mendili, Y.; Karakurt, G.; Grambow, B.; Martin, C. Corrosion of carbon steel under sequential aerobic-anaerobic environmental conditions. *Corrosion Science* **2013,** *76*, 432-440.

(6) Marques Fernandes, M.; Ver, N.; Baeyens, B. Predicting the uptake of Cs, Co, Ni, Eu, Th and U on argillaceous rocks using sorption models for illite. *Applied Geochemistry* **2015,** *59*, 189-199.

(7) Karnland, O. *Chemical and mineralogical characterization of the bentonite buffer for the acceptance control procedure in a KBS-3 repository*; Technical Report SKB TR-10-60: 2010.

(8) Myneni, S. C. B.; Tokunaga, T. K.; Brown, G. E. Abiotic selenium redox transformations in the presence of Fe(II,III) oxides. *Science* **1997,** *278*, 1106-1109.

(9) Scheinost, A. C.; Charlet, L. Selenite reduction by mackinawite, magnetite and siderite: XAS characterization of nanosized redox products. *Environ. Sci. Technol.* **2008,** *42* (6), 1984–1989.

(10) Jaisi, D. P.; Dong, H.; Plymale, A. E.; Fredrickson, J. K.; Zachara, J. M.; Heald, S.; Liu, C. Reduction and long-term immobilization of technetium by Fe(II) associated with clay mineral nontronite. *Chemical Geology* **2009,** *264* (1-4), 127-138.

(11) Kirsch, R.; Fellhauer, D.; Altmaier, M.; Neck, V.; Rossberg, A.; Fanghänel, T.; Charlet, L.; Scheinost, A. C. Oxidation state and local structure of plutonium reacted with magnetite, mackinawite and chukanovite. *Environ. Sci. Technol.* **2011,** *45* (17), 7267–7274.

(12) Um, W.; Chang, H.-S.; Icenhower, J. P.; Lukens, W. W.; Serne, R. J.; Qafoku, N. P.; Westsik, J. H., Jr.; Buck, E. C.; Smith, S. C. Immobilization of 99-Technetium (VII) by Fe(II)-Goethite and Limited Reoxidation. *Environmental Science & Technology* **2011,** *45* (11), 4904-4913.

(13) Huber, F.; Schild, D.; Vitova, T.; Rothe, J.; Kirsch, R.; Schafer, T. U(VI) removal kinetics in presence of synthetic magnetite nanoparticles. *Geochim. Cosmochim. Ac.* **2012,** *96*, 154-173.

(14) Peretyazhko, T. S.; Zachara, J. M.; Kukkadapu, R. K.; Heald, S. M.; Kutnyakov, I. V.; Resch, C. T.; Arey, B. W.; Wang, C. M.; Kovarik, L.; Phillips, J. L.; Moore, D. A. Pertechnetate (TcO4-) reduction by reactive ferrous iron forms in naturally anoxic, redox transition zone sediments from the Hanford Site, USA. *Geochimica Et Cosmochimica Acta* **2012,** *92*, 48-66.

(15) Magill, J.; Pfennig, G.; Galy, J. *Chart of the nuclides*. 7th ed.; European Commission - DG Joint Research Centre - Institute of Transuranium Elements: Karlsruhe, 2006; p 44.

(16) Runde, W. The Chemical Interactions of Actinides in the Environment. *Los Alamos Science* **2000,** (26), 392-411.

(17) Dardenne, K.; Seibert, A.; Denecke, M. A.; Marquardt, C. M. Plutonium(III,IV,VI) speciation in Gorleben groundwater using XAFS. *Radiochim. Acta* **2009,** *97* (2), 91-97.

(18) Rothe, J.; Walther, C.; Denecke, M. A.; Fanghanel, T. XAFS and LIBD investigation of the formation and structure of colloidal Pu(IV) hydrolysis products. *Inorg. Chem.* **2004,** *43* (15), 4708-4718.

(19) Rai, D.; Gorby, Y. A.; Fredrickson, J. K.; Moore, D. A.; Yui, M. Reductive dissolution of PuO_2(am): The effect of Fe(II) and hydroquinone. *J. Solution Chem.* **2002,** *31* (6), 433-453.

(20) Felmy, A. R.; Moore, D. A.; Rosso, K. M.; Qafoku, O.; Rai, D.; Buck, E. C.; Ilton, E. S. Heterogeneous reduction of PuO_2 with Fe(II): importance of the Fe(III) reaction product. *Environ. Sci. Technol.* **2011,** *45*, 3952-3958.

(21) Powell, B. A.; Fjeld, R. A.; Kaplan, D. I.; Coates, J. T.; Serkiz, S. M. $Pu(V)O_2^+$ adsorption and reduction by synthetic hematite and goethite. *Environmental Science & Technology* **2005,** *39* (7), 2107-2114.

(22) Powell, B. A.; Fjeld, R. A.; Kaplan, D. I.; Coates, J. T.; Serkiz, S. M. $Pu(V)O_2^+$ adsorption and reduction by synthetic magnetite (Fe_3O_4). *Environ. Sci. Technol.* **2004,** *38* (22), 6016-6024.

(23) Kersting, A. B.; Zhao, P.; Zavarin, M.; Sylwester, E. R.; Allen, P. G.; Williams, R. W., Sorption of Pu(V) on Mineral Colloids. In *Colloidal-Facilitated Transport of Low-Solubility Radionuclides: A Field, Experimental, and Modeling Investigation; Report UCRL-ID-149688*, Kersting A. B., R., P. W., Ed. Lawrence Livermore National Laboratory, Livermore, CA: 2003.

(24) Sanchez, A. L.; Murray, J. W.; Sibley, T. H. The adsorption of plutonium IV and V on goethite. *Geochim. Cosmochim. Acta* **1985,** *49*, 2297-2307.
(25) Keeney-Kennicutt, W. L.; Morse, J. W. The redox chemistry of $Pu(V)O_2^+$ interaction with common mineral surfaces in dilute solutions and seawater. *Geochim. Cosmochim. Acta* **1985,** *49*, 2577-2588.
(26) Duro, L.; El Aamrani, S.; Rovira, M.; De Pablo, J.; Bruno, J. Study of the interaction between U(VI) and the anoxic corrosion products of carbon steel. *Appl. Geochem.* **2008,** *23*, 1094-1100.
(27) White, A. F.; Peterson, M. L. Reduction of aqueous transition metal species on the surfaces of Fe(II)-containing oxides. *Geochim. Cosmochim. Acta* **1996,** *60* (20), 3799-3814.
(28) Moon, J. W.; Roh, Y.; Yeary, L. W.; Lauf, R. J.; Rawn, C. J.; Love, L. J.; Phelps, T. J. Microbial formation of lanthanide-substituted magnetites by Thermoanaerobacter sp TOR-39. *Extremophiles* **2007,** *11* (6), 859-867.
(29) De Silva, C. R.; Smith, S.; Shim, I.; Pyun, J.; Gutu, T.; Jiao, J.; Zheng, Z. P. Lanthanide(III)-Doped Magnetite Nanoparticles. *Journal of the American Chemical Society* **2009,** *131* (18), 6336–6337.
(30) Nedel, S.; Dideriksen, K.; Christiansen, B. C.; Bovet, N.; Stipp, S. L. S. Uptake and Release of Cerium During Fe-Oxide Formation and Transformation in Fe(II) Solutions. *Environmental Science & Technology* **2010,** *44* (12), 4493-4498.
(31) Duff, M. C.; Coughlin, J. U.; Hunter, D. B. Uranium co-precipitation with iron oxide minerals. *Geochimica Et Cosmochimica Acta* **2002,** *66* (20), 3533-3547.
(32) Ilton, E. S.; Pacheco, J. S. L.; Bargar, J. R.; Shi, Z.; Liu, J.; Kovarik, L.; Engelhard, M. H.; Felmy, A. R. Reduction of U(VI) Incorporated in the Structure of Hematite. *Environmental Science & Technology* **2012,** *46* (17), 9428-9436.
(33) Boland, D. D.; Collins, R. N.; Payne, T. E.; Waite, T. D. Effect of Amorphous Fe(III) Oxide Transformation on the Fe(II)-Mediated Reduction of U(VI). *Environmental Science & Technology* **2011,** *45* (4), 1327-1333.
(34) Nico, P. S.; Stewart, B. D.; Fendorf, S. Incorporation of Oxidized Uranium into Fe (Hydr)oxides during Fe(II) Catalyzed Remineralization. *Environmental Science & Technology* **2009,** *43* (19), 7391-7396.
(35) Stewart, B. D.; Nico, P. S.; Fendorf, S. Stability of Uranium Incorporated into Fe (Hydr)oxides under Fluctuating Redox Conditions. *Environmental Science & Technology* **2009,** *43* (13), 4922-4927.
(36) Nakata, K.; Nagasaki, S.; Tanaka, S.; Sakamoto, Y.; Tanaka, T.; Ogawa, H. Sorption and reduction of neptunium(V) on the surface of iron oxides. *Radiochimica Acta* **2002,** *90* (9-11), 665-669.
(37) Nakata, K.; Nagasaki, S.; Tanaka, S.; Sakamoto, Y.; Tanaka, T.; Ogawa, H. Reduction rate of neptunium(V) in heterogeneous solution with magnetite. *Radiochimica Acta* **2004,** *92* (3), 145-149.
(38) Moyes, L. N.; Jones, M. J.; Reed, W. A.; Livens, F. R.; Charnock, J. M.; Mosselmans, J. F. W.; Hennig, C.; Vaughan, D. J.; Pattrick, R. A. D. An X-ray absorption spectroscopy study of neptunium(V) reactions with mackinawite (FeS). *Environ. Sci. Technol.* **2002,** *36* (2), 179-183.
(39) Christiansen, B. C.; Geckeis, H.; Marquardt, C. M.; Bauer, A.; Roemer, J.; Wiss, T.; Schild, D.; Stipp, S. L. S. Neptunyl (NpO2+) interaction with green rust, GR(Na,SO4). *Geochimica Et Cosmochimica Acta* **2011,** *75* (5), 1216-1226.
(40) Frohlich, D. R.; Amayri, S.; Drebert, J.; Grolimund, D.; Huth, J.; Kaplan, U.; Krause, J.; Reich, T. Speciation of Np(V) uptake by Opalinus Clay using synchrotron microbeam techniques. *Anal. Bioanal. Chem.* **2012,** *404* (8), 2151-2162.
(41) Brookshaw, D. R.; Pattrick, R. A. D.; Bots, P.; Law, G. T. W.; Lloyd, J. R.; Mosselmans, J. F. W.; Vaughan, D. J.; Dardenne, K.; Morrie, K. Redox Interactions of Tc(VII), U(VI), and Np(V) with Microbially Reduced Biotite and Chlorite. *Environmental Science & Technology* **2015,** *49* (22), 13139-13148.
(42) Wylie, E. M.; Olive, D. T.; Powell, B. A. Effects of Titanium Doping in Titanomagnetite on Neptunium Sorption and Speciation. *Environmental Science & Technology* **2016,** *50* (4), 1853-1858.
(43) Rossberg, A.; Reich, T.; Bernhard, G. Complexation of uranium(VI) with protocatechuic acid - application of iterative transformation factor analysis to EXAFS spectroscopy. *Anal. Bioanal. Chem.* **2003,** *376* (5), 631-638.
(44) Zavarin, M.; Roberts, S. K.; Hakem, N.; Sawvel, A. M.; Kersting, A. B. Eu(III), Sm(III), Np(V), Pu(V), and Pu(IV) sorption to calcite. *Radiochimica Acta* **2005,** *93* (2), 93-102.
(45) Tits, J.; Wieland, E.; Bradbury, M. H.; Eckert, P.; Schaible, A. *The Uptake of Eu(lll) and Th(IV) by Calcite under Hyperalkaline Conditions.* ; PSI Bericht Nr. 02-03: Villigen, Switzerland, 2002.
(46) Husar, R.; Hübner, R.; Hennig, C.; Martin, P. M.; Chollet, M.; Weiss, S.; Stumpf, T.; Zänker, H.; Ikeda-Ohno, A. Intrinsic formation of nanocrystalline neptunium dioxide under neutral aqueous conditions relevant to deep geological repositories. *Chemical Communications* **2015,** *51* (7), 1301-1304.
(47) Hennig, C. Evidence for double-electron excitations in the L_3-edge x-ray absorption spectra of actinides. *Phys. Rev. B* **2007,** *75* (035120), 035120-1 - 035120-7.
(48) Funke, H.; Scheinost, A. C.; Chukalina, M. Wavelet analysis of extended X-ray absorption fine structure data. *Physical Review* **2005,** *B 71*, 094110.

(49) Lemire, R. J.; Fuger, J.; Nitsche, H.; Potter, P.; Rand, M. H.; Rydberg, J.; Spahiu, K.; Sullivan, J. C.; Ullmann, W. J.; Vitorge, P.; Wanner, H. *Chemical Thermodynamics of Neptunium and Plutonium*. Elsevier: Amsterdam, 2001; p 870.
(50) Guillaumont, R.; Fanghänel, T.; Fuger, J.; Grenthe, I.; Neck, V.; Palmer, D. A.; Rand, M. H. *Update on the Chemical Thermodynamics of Uranium, Neptunium, Plutonium, Americium and Technetium*. Elsevier: Amsterdam, 2003.
(51) Zachariasen, W. H. Crystal chemical studies of the 5f-series of elements: XII. New compounds representing known structure type. *Acta Crystallographica* **1949,** *2*, 388-390.
(52) Rothe, J.; Denecke, M. A.; Neck, V.; Muller, R.; Kim, J. I. XAFS investigation of the structure of aqueous thorium(IV) species, colloids, and solid thorium(IV) oxide/hydroxide. *Inorg Chem* **2002,** *41* (2), 249-258.
(53) Ikeda-Ohno, A.; Hennig, C.; Tsushima, S.; Scheinost, A. C.; Bernhard, G.; Yaita, T. Speciation and structural study of U(IV) and -(VI) in perchloric and nitric acid solutions. *Inorg. Chem.* **2009,** *48* (15), 7201-7210.
(54) Taylor, D. Thermal-expansion data. 2. Binary oxide with the fluorite and rutile structures, MO_2, and the antifluorite structure, M_2O. *Transactions and Journal of the British Ceramic Society* **1984,** *83* (2), 32-37.
(55) Hennig, C.; Ikeda-Ohno, A.; Emmerling, F.; Kraus, W.; Bernhard, G. Comparative investigation of the solution species $[U(CO3)_5]^{6-}$ and the crystal structure of $Na_6[U(CO3)_5]$ $12H_2O$. *Dalton Trans.* **2010,** *39* (15), 3744-3750.
(56) Clark, D. L.; Conradson, S. D.; Keogh, D. W.; Palmer, P. D.; Scott, B. L.; Tait, C. D. Identification of the limiting species in the plutonium(IV) carbonate system. Solid state and solution molecular structure of the Pu(CO3)(5) (6-) ion. *Inorg Chem* **1998,** *37* (12), 2893-2899.
(57) Baeyens, B.; Thoenen, T.; Bradbury, M. H.; Marques Fernandes, M. *Sorption Data Bases for Argillaceous Rocks and Bentonite for the Provisional Safety Analysis for SGT-E2*; Nagra: Wettingen, Switzerland, 2014.
(58) Latta, D. E.; Gorski, C. A.; Boyanov, M. I.; O'Loughlin, E. J.; Kemner, K. M.; Scherer, M. M. Influence of Magnetite Stoichiometry on U-VI Reduction. *Environmental Science & Technology* **2012,** *46* (2), 778-786.
(59) Veeramani, H.; Scheinost, A. C.; Monsegue, N.; Qafoku, N. P.; Kukkadapu, R.; Newville, M.; Lanzirotti, A.; Pruden, A.; Murayama, M.; Hochella Jr., M. F. Abiotic reductive immobilization of U(VI) by biogenic mackinawite. *Environ. Sci. Technol.* **2013,** *47*, 2361-2369.
(60) Zanker, H.; Hennig, C. Colloid-borne forms of tetravalent actinides: A brief review. *J. Contam. Hydrol.* **2014,** *157*, 87-105.
(61) Kim, B. Y.; Oh, J. Y.; Baik, M. H.; Yun, J. I. Effect of carbonate on the solubility of neptunium in natural granitic groundwater. *Nuclear Engineering and Technology* **2010,** *42* (5), 552-561.
(62) Kitamura, A.; Kohara, Y. Carbonate complexation of neptunium(IV) in highly basic solutions. *Radiochimica Acta* **2004,** *92* (9-11), 583-588.
(63) Walther, C.; Denecke, M. A. Actinide Colloids and Particles of Environmental Concern. *Chemical Reviews* **2013,** *113* (2), 995-1015.
(64) Kersting, A. B. Plutonium Transport in the Environment. *Inorg Chem* **2013,** *52* (7), 3533-3546.
(65) Liger, E.; Charlet, L.; Van Cappellen, P. Surface catalysis of uranium(VI) reduction by iron(II). *Geochimica et Cosmochimica Acta* **1999,** *63* (19/20), 2939-2955.
(66) Husar, R.; Weiss, S.; Hennig, C.; Hübner, R.; Ikeda-Ohno, A.; Zänker, H. Formation of neptunium(IV)−silica colloids at near-neutral and slightly alkaline pH. *Environ. Sci. Technol.* **2015,** *49*, 665−671.
(67) Scheinost, A. C.; Kirsch, R.; Banerjee, D.; Fernandez-Martinez, A.; Zaenker, H.; Funke, H.; Charlet, L. X-ray absorption and photoelectron spectroscopy investigation of selenite reduction by FeII-bearing minerals. *J. Contam. Hydrol.* **2008,** *102* (3-4), 228-245.
(68) Bedlivy, D.; Preisinger, A. Die Struktur von $Na_2S \cdot 9H_2O$ und $Na_2Se \cdot 9H_2O$. *Zeitschrift für Kristallographie* **1965,** *121* (2-4), 114-130.
(69) Rousselot, I.; Taviot-Gueho, C.; Leroux, F.; Leone, P.; Palvadeau, P.; Besse, J. P. Insights on the structural chemistry of hydrocalumite and hydrotalcite-like materials: Investigation of the series $Ca_2M^{3+}(OH)_6Cl$ $x2H_2O$ (M^{3+}: Al^{3+}, Ga^{3+}, Fe^{3+}, and Sc^{3+}) by X-ray powder diffraction. *Journal of Solid State Chemistry* **2002,** *167* (1), 137-144.
(70) Cherin, P.; Unger, P. Refinement of the crystal structure of alpha-monoclinic Se. *Acta Crystallogr., B* **1972,** *28*, 313-317.
(71) Charlet, L.; Scheinost, A. C.; Tournassat, C.; Greneche, J.-M.; Géhin, A.; Fernández-Martínez, A.; Coudert, S.; Tisserand, D.; Brendle, J. Electron transfer at the mineral/water interface: Selenium reduction by ferrous iron sorbed on clay. *Geochim. Cosmochim. Ac.* **2007,** *71* (23), 5731-5749.

2.2 Zahlenmäßiger Nachweis

Die wichtigsten Punkte des zahlenmäßigen Nachweises über die Verwendung der Zuwendungen an HZDR-IRE sind:

- **221.890,91 € Personalkosten**
- **2.866,39 € Materialkosten**
- **29.721,53 € Reisekosten** (siehe Tabelle 2)
- **14.133,46 € Transportkosten**

2.3 Notwendigkeit und Angemessenheit der geleisteten Arbeit

Ohne die hier beantragten Mittel hätte das geplante Vorhaben nicht durchgeführt werden können, da es keine alternativen Fördermöglichkeiten für dieses Verbundvorhaben auf lokaler, regionaler, nationaler oder europäischer Ebene gegeben hat. Die in Rechnung gestellten Verbrauchsmaterialien und Chemikalien wurden für die Durchführung der experimentellen Arbeiten benötigt.

Die Personalkosten wurden für die Durchführung der experimentellen, analytischen Arbeiten, Auswertung der Messungen, für Modellierungsarbeiten und für die Zusammenfassung in Form von Publikationen und Berichten verwendet.

Die Reisekosten wurden ausschließlich für die Teilnahme an den jährlichen Statusseminaren, Reisen zu Messzeiten an Synchrotron- Strahlungsquellen, Forschungsaufenthalte und der Teilnahme an nationalen/internationalen Fachtagungen verwendet.

2.4 Verwertbarkeit der Ergebnisse (vgl. Verwertungsplan)

Der Verwertungsplan sieht die Publikation der wissenschaftlichen Ergebnisse vor.

Einige der in Abschnitt 2.1.2 dargestellten Ergebnisse sind bereits in internationalen Fachjournals mit *„peer review“* publiziert. Eine komplette Auflistung aller relevanten Publikationen findet sich in Kapitel 2.6.

2.5 Fortschritt bei anderen Stellen

Hier sind keine Angaben zu machen.

2.6 Erfolgte oder geplante Veröffentlichungen

Bisher wurde eine Publikation in Environmental Science & Technology mit sehr hohem Impact Factor (5.8) im Kontext des ImmoRad Projekts veröffentlicht. Zwei weitere sind bei Geochimica Cosmochimica Acta und Environmental Science & Technology eingereicht, drei weitere sind in der Vorbereitungsphase und werden entweder noch in 2016 oder in der ersten Jahreshälfte 2017 eingereicht. Diese sind im Detail:

Veröffentlichungen mit peer-review:

Börsig, N.; Scheinost, A. C.; Shaw, S.; Schild, D.; Neumann, T., 2016. Uptake mechanisms of selenium oxyanions during the ferrihydrite-hematite recrystallization. *Geochimica Cosmochimica Acta* **206**, 236-253

Scheinost, A. C., Steudtner, R., Hübner, R., Weiss, S., and Bok, F., 2016. Neptunium^{V} retention by siderite under anoxic conditions: Precipitation of NpO_2–like nanoparticles and of Np^{IV} pentacarbonate. *Environmental Science & Technology* **50**, 10413-10420.

Geplante/eingereichte Veröffentlichungen:

Dumas, T., Fellhauer, D., Gaona, X., and Scheinost, A. C., 2017. Molecular mechanisms of Pu reductive sorption and precipitation at the magnetite/water interface. *Environmental Science & Technology*, submitted.

Rojo, H., Scheinost, A. C., Lothenbach, B., A., L., Wieland, E., and Tits, J., 2017. Uptake of selenium(-II) by calcium aluminate hydrate (AFm) phases under alkaline conditions. *Environmental Science & Technology*, submitted.

Steudtner, R., Hübner, R., Weiss, S., and Scheinost, A. C., 2016. Molecular mechanisms of Np reductive sorption and precipitation at the mackinawite/water interface. *Environmental Science & Technology*, in preparation.

Steudtner, R., Hübner, R., and Weiss, S., and Scheinost, A. C., 2016. Molecular mechanisms of Np reductive sorption and precipitation at the magnetite/water interface. *Environmental Science & Technology*, in preparation.

Beiträge zu Konferenzen und Workshops:

Keynote

Breynaert, E., Dom, D., Scheinost, A.C., Kirschhock, C.E.A., Maes, A. 2012. Interaction of selenite with iron sulphide minerals: a new perspective. Goldschmidt Conference 2012, 24. – 29.06.2012, Montreal, Canada.

Invited

Scheinost, A.C., Kirsch, R., Dumas, T., Rossberg, A., Fellhauer, D., Gaona, X., Altmaier, M. 2013. Interaction of plutonium with magnetite under anoxic conditions: Reduction, surface complexation, and structural incorporation. Actinides-Conference, 21.-26.07.2013, Karlsruhe

Scheinost, A.C.; Dumas, T.; Steudtner, R.; Fellhauer, D.; Gaona, X.; Altmaier, M. 2014. Interaction of plutonium and neptunium with magnetite under anoxic conditions: Reduction, surface complexation, and structural incorporation. Actinide XAS 2014, 20.-22.05.2014, Schloss Boettstein, Switzerland

Scheinost, A.C., Kirsch, R., Dumas, T., Rossberg, A., Fellhauer, D., Gaona, X., Altmaier, M. 2014. Interaction of plutonium with magnetite under anoxic conditions: Reduction, surface complexation, and structural incorporation. 248th ACS National Meeting, 10.-14.08.2014, San Francisco, USA

Wieland, E., Rojo, H., Scheinost, A.C., Lothenbach, B., Tits, J., 2015. Redox transformations and the disposal of radioactive waste: Influence on Se immobilization. Goldschmidt Conference, 16.-21.08.2015, Prague, Czech Republic

Contributed

Kirsch, R., Fellhauer, D., Altmaier, M., Charlet, L., Fanghaenel, T., Scheinost, 2012. Plutonium redox chemistry under anoxic conditions in the presence of iron(II) bearing minerals. Goldschmidt Conference 2012, 24. – 29.06.2012, Montreal, Canada.

Dumas, T., Fellhauer, D., Gaona, X., Altmaier, M., Scheinost, A.C. 2013. Is plutonium being incorporated by magnetite under anoxic conditions? Mineralogical Magazine, 77(5) 1017 und Goldschmidt Conference, 25.-30.08.2013, Florence, Italy.

Rojo, H., Tits, J., Scheinost, A. C., Wieland, E. 2014. Retention of selenium by cementitious materials under the reducing conditions prevailing in a radioactive waste repository. Goldschmidt Conference, 8 – 13.06.2014, Sacramento, USA.

Rojo, H., Tits j., Scheinost, A.C., Wieland, E. 2014. Retention of selenium by cementitious materials under anoxic and reducing conditions. IGTDP Geodisposal Conference, 24 – 26.06.2014, Manchester, UK.

Rojo, H., Tits, J., Scheinost, A.C., Wieland, E. 2014. Retention of selenium by cementitious materials under oxidizing and reducing conditions, Selen2014, 13 – 14.10 2014, Karlsruhe, Germany.

Steudtner, R., Hübner, R., Müller, K., Weiss, S., Scheinost, A.C. 2015. Neptunium Redox Reactions at the Iron Mineral − Water Interface. Goldschmidt Conference, 16.-21.08.2015, Prague, Czech Republic

Rojo. H., Scheinost, A.C., Tits, J., Lothenbach, B., Wieland, E. 2015. Redox transformations and the disposal of radioactive waste: Influence on the Se immobilisation. Goldschmidt Conference 2015, 16 – 21.08.2015, Prague, Czech Republic.

Sessions bei internationalen Konferenzen:

Goldschmidtkonferenz 2012, Montreal Kanada:

Session 8a. Mineral growth and dissolution: modern approaches to molecular-level reaction mechanism determination with implications for toxic metal sequestration, biomineralization, and engineering

Convenors: Andrew Stack (Oak Ridge National Laboratory), Steve Higgins (Wright State University), Frank Heberling (Karlsruhe Institute of Technology)

Session 8c. Structural incorporation of heavy metals/radionuclides into mineral phases in aqueous environment

Convenors: Thorsten Stumpf (Karlsruhe Institute of Technology), Thomas Neumann (Karlsruhe Institute of Technology)

Goldschmidtkonferenz 2013, Florenz Italien:

Session 18i: Interaction of Oxyanions with Mineral Phases: Sorption, Redox Transformation, and Structural Incorporation

Convenors: Andreas C. Scheinost (Helmholtz Zentrum Dresden Rossendorf), Thomas Neumann & Thorsten Schäfer (Karlsruhe Institute of Technology), Laurent Charlet (University of Grenoble/ CNRS)

Goldschmidtkonferenz 2015, Prag, Tschechische Republik:

13e: Biogeochemical Redox Processes and Radiocontaminants

Convenors: Andreas C. Scheinost (Helmholtz Zentrum Dresden Rossendorf), Mavrik Zavarin (LLNL), Katherine Morris (Univ. Manchester) & Maria Marques Fernandes (PSI)

Berichtsblatt

1. ISBN oder ISSN	2. Berichtsart (Schlussbericht oder Veröffentlichung) Abschlussbericht

3a. Titel des Berichts

Grundlegende Untersuchungen zur Immobilisierung langlebiger Radionuklide durch die Wechselwirkung mit endlagerrelevanten Sekundärphasen

3b. Titel der Publikation

4a. Autor(en) [Name(n), Vorname(n)] des Berichts Scheinost, Andreas C.; Dumas, Thomas; Steudtner, Robin; Dulnee, Siriwan	5. Abschlussdatum des Vorhabens September 2015
4b. Autor(en) [Name(n), Vorname(n)] der Publikation	7. Form der Publikation
8. Durchführende Institution(en) (Name, Adresse) Helmholtz Zentrum Dresden Rossendorf e.V. (HZDR) Institut für Ressourcenökologie (IfR) Bautzner Landstrasse 400 01328 Dresden	9. Ber. Nr. Durchführende Institution
	10. Förderkennzeichen 02NUK019D
	11. Seitenzahl Bericht 40
	11b. Seitenzahl Publikation
12. Fördernde Institution (Name, Adresse) Bundesministerium für Bildung und Forschung (BMBF) 53170 Bonn	13. Literaturangaben 71
	14. Tabellen 3
	15. Abbildungen 20

16. Zusätzliche Angaben

17. Vorgelegt bei (Titel, Ort, Datum)

18. Kurzfassung

Ziel des vorliegenden Projektes war es, die Rückhaltung von Neptunium(V) und Plutonium(V) an Fe(II)-haltigen Mineralen (Magnetit, Mackinawit, Siderit), die sich im Endlager als Korrosionsprodukte bilden können, auf molekularer Ebene mittels Röntgenabsorptionsspektroskopie (XAFS) zu untersuchen. Im Fokus standen dabei Sorptions-, Redox- und Ausfällungsreaktionen, die zur Bildung von Festen Phasen führen können. Kopräzipitationsexperimente im System Pu/Magnetit bestätigten diese Hypothese, indem erhebliche Mengen an Pu (2500 mg/kg) in dreiwertiger Oxidationsstufe in der Oh-Position in Magnetit eingebaut wurden. Allerdings wurde die Hälfte des Pu durch Fe(II)-beschleunigte Mineralalterung wieder freigesetzt und anschließend an den {111} Mineraloberflächen durch Bildung eines tridentaten Sorptionskomplexes adsorbiert. Daher kann der strukturelle Einbau von Pu(III) zwar kinetisch forciert werden; wegen seiner strukturellen Inkompatibilität ist das eingebaute Pu(III) aber thermodynamisch ungünstig und damit langfristig nicht stabil. Im Gegensatz dazu ist der hochsymmetrische Pu(III) Oberflächenkomplex, der sich innerhalb einer Stunde bildet, auch nach zwei Jahren noch stabil und stellt vermutlich die für die Endlagersicherheit relevante Gleichgewichtsphase dar.

Im Gegensatz zu Plutonium wurde Neptunium(V) von den untersuchten Fe(II)-Mineralen wie erwartet nur zur vierwertigen Oxidationsstufe reduziert. Im Np/Magnetit-System bildete sich dabei sowohl eine nanopartikuläre NpO_2-aehnliche Phase als auch ein tridentater mononuklearer Sorptionskomplex, wobei letzterer bei kurzen (1 h) Reaktionszeiten und pH 6 überwiegt, ersterer dagegen bei pH 12 und längeren (3 Wochen) Reaktionszeiten. Einbau von Np(IV) in Magnetit wurde nicht beobachtet. Im Np/Siderit-System bildete sich nur nanopartikuläres NpO_2; im Gegensatz zu Magnetit kann sich bei Siderit kein Sorptionskomplex ausbilden, der stabil genug wäre, um die Löslichkeits-dominierte NpO_2-Ausfällung zu verhindern. Ebenso wenig wie bei Magnetit wurde bei Siderit ein struktureller Einbau von Np(IV) beobachtet; allerdings wurde bei den Kopräzipitationsexperimenten erstmalig eine Np(IV)-Pentakarbonat-Festphase gefunden. Im Np/Mackinawit-System konnte eine früher gefundene Np-S-Koordination nicht bestätigt werden; stattdessen bildete sich ein Gemisch aus NpO_2-Nanopartikeln und einem O-koordinierten Sorptionskomplex an einer sekundären Fe-Oxid-Phase. Ein Einbau in die Mackinawit-Struktur fand nicht statt.

Zusammenfassen kann gesagt werden, dass die untersuchten Korrosionsminerale Neptunium und Plutonium vollständig und schnell reduzieren, und durch die Ausbildung von Sorptionskomplexen bzw. durch Ausfällung von NpO_2 Nanopartikeln die Löslichkeit des wegen ihrer langlebigen Radionuklide problematischen Neptuniums und Plutoniums stark reduzieren. Während reine NpO_2-Nanopartikel kaum zur Kolloidbildung neigen, könnte die Bildung von Silikat-reichen NpO_2-Nanopartikeln eventuell zu stabilen Kolloidsuspensionen und damit zu einem verstärkten Transport von Np führen. In allen anderen Fällen sollte die Stahlhülle selbst nach dem Durchrosten durch die Ausbildung einer Barriere aus hochreaktiven Fe(II)-Mineralen die Migration von Np und Pu stark hemmen. Die strukturelle Inkorporation und die Bildung fester Phasen scheint bei diesen Rückhaltungsprozessen aber nur eine relativ geringe Rolle zu spielen, im Gegensatz zu den Spaltprodukte Se und Tc.

19. Schlagwörter

Feste Lösungen, Radionuklide, Sekundärphasen, Redoxprozesse, Sorption, Magnetit, Mackinawit, Siderit, Pu, Np

20. Verlag	21. Preis

Document Control Sheet

1. ISBN or ISSN	2. type of document (e.g. report, publication) Final report
3. title Fundamental studies on the immobilizing of long-lived radionuclides by the interaction with repository-relevant secondary phases.	
4. author(s) (family name, first name(s)) Scheinost, Andreas C.; Dumas, Thomas; Steudtner, Robin; Dulnee, Siriwan	5. end of project September 2015
	6. publication date
	7. form of publication
8. performing organization(s) (name, address) Helmholtz Zentrum Dresden Rossendorf e.V. (HZDR) Institut für Ressourcenökologie (IfR) Bautzner Landstrasse 400 01328 Dresden	9. originator's report no.
	10. reference no. 02NUK019D
	11. no. of pages 40
12. sponsoring agency (name, address) Bundesministerium für Umwelt, Naturschutz und Reaktorsicherheit (BMU) Alexanderstraße 3 10178 Berlin	13. no. of references 71
	14. no. of tables 3
	15. no. of figures 20
16. supplementary notes	
17. presented at (title, place, date)	

18. abstract

Goal of the current project was to investigate the retention of Np(V) and Pu(V) by Fe(II)-bearing minerals (magnetite, mackinawite, siderite), which form as corrosion products in nuclear waste repositories, at the molecular level by X-ray absorption fine structure (XAFS) spectroscopy. The focus was thereby on sorption, redox and precipitation reactions, which may possibly lead to the formation of solid solutions. Coprecipitation experiments in the Pu/magnetite system supported this hypothesis, since substantial amounts of Pu (2500 mg/kg) at the trivalent oxidation state were structurally incorporated at the Oh position of magnetite. Half of this incorporated Pu was, however, released by the Fe(II)-enforced mineral aging, and then re-adsorbed at the magnetite {111} faces by forming a tridentate inner-sphere sorption complex. Hence the structural incorporation of Pu(III) by magnetite can be enforced kinetically; due to its structural incompatibility it is, however, thermodynamically not favorable and hence instable on the long term. In contrast is the highly symmetrical Pu(III) surface complex, which forms within one hour, even after 2 years still stable, thereby most likely representing the equilibrium phase relevant for the safety case of nuclear waste repositories.

In contrast to Pu, Np(V) was reduced as expected only to the tetravalent oxidation state by the Fe(II)-bearing minerals. In the Np/magnetite system we observed formation of a nanoparticulate NpO_2-like phase as well as of a tridentate mononuclear sorption complex, the latter prevailing after short (1 h) reaction times and pH 6, the former at pH 12 and longer (3 weeks) reaction time. The structural incorporation of Np(IV) by magnetite was not observed. In the Np/siderite system only NpO_2 nanoparticles formed; in contrast to magnetite, Np(IV) does not form a sorption complex with siderite, which is strong enough to compete with the solubility-determined precipitation of NpO_2 nanoparticles. Like for magnetite, no structural incorporation of Np(IV) in siderite was observed. We observed during the coprecipitation experiments, however, for the first time the formation of a Np(IV) pentacarbonate solid, analogous to the previously identified U(IV) and Pu(IV) pentacarbonates. In the Np/mackinawite system we could not confirm the previously found Np-S coordination; instead, we observed a mixture of nanoparticulate NpO_2 and of a O-coordinated Np(IV) sorption complex with a secondary Fe oxide phase. Structural incorporation did not take place.

In conclusion, the investigated corrosion minerals reduced Np and Pu completely and rapidly; by formation of inner-sphere sorption complexes and the precipitation of NpO_2 nanoparticles, the solubility of both Np and Pu was greatly reduced. While pure NpO_2 nanoparticles do not tend to form colloids, formation of silicate-rich NpO_2 nanoparticles may form stable colloidal suspensions and hence increase Np transportation. In all other cases, however, the steel containers should strongly retard Np and Pu migration even after their corrosion by forming a barrier of highly reactive Fe(II) minerals. The structural incorporation and formation of solid solutions seems to play only a small role for such attenuation processes, in contrast to their relevance for the retention of the fission products Se and Tc.

19. keywords

Solid solutions, radionuclides, secondary phases, redox processes, sorption, magnetite, mackinawite, siderite, Pu, Np

20. publisher	21. price